Cell

The Fanconi anemia pathway induces chromothripsis and ecDNA-driven cancer drug resistance

Graphical abstract

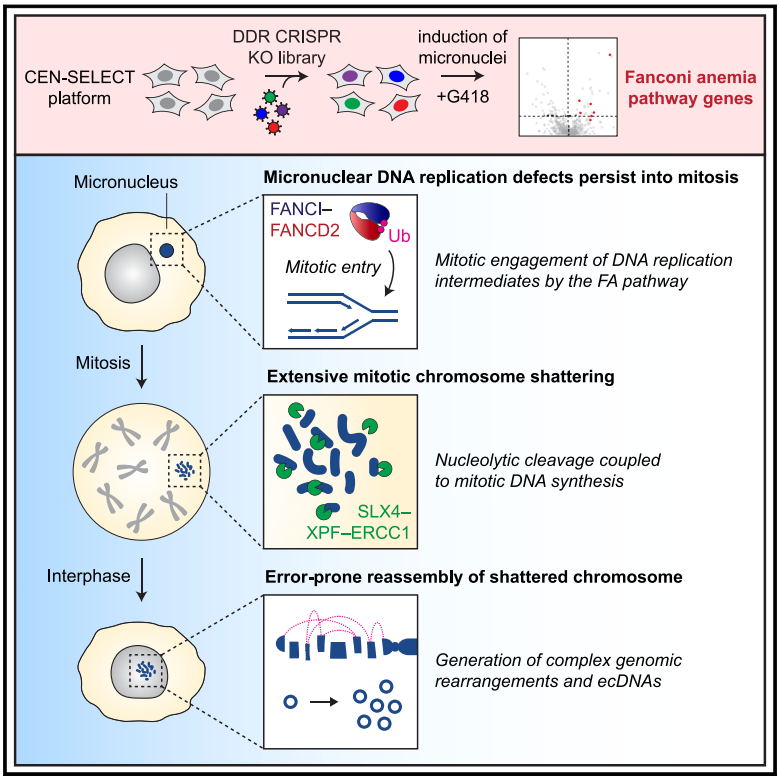

Highlights

- The FA pathway promotes the catastrophic shattering of micronuclear chromosomes
- SLX4-XPF-ERCC1 cleaves mitotic DNA replication intermediates from micronuclei
- MiDAS facilitates the mutagenic reassembly of shattered chromosomes in interphase
- FA-induced mitotic shattering drives genome rearrangements and ecDNA formation

Authors

Justin L. Engel, Xiao Zhang, Mingming Wu, ..., Isidro Cortés-Ciriano, Roger S. Lo, Peter Ly

Correspondence

peter.ly@utsouthwestern.edu

In brief

A genetic screen uncovers the Fanconi anemia pathway as a driver of chromothripsis by shattering under-replicated micronuclear chromosomes during mitosis. This process involves chromosome-scale cleavage by the SLX4-XPF-ERCC1 endonuclease coupled to mitotic DNA synthesis, resulting in complex rearrangements and ecDNAs that fuel cancer genome evolution and/or resistance to anti-cancer therapies.

Engel et al., 2024, Cell *187*, 6055–6070
October 17, 2024
https://doi.org/10.1016/j.cell.2024.08.001

CellPress

Cell

CellPress

Article

The Fanconi anemia pathway induces chromothripsis and ecDNA-driven cancer drug resistance

Justin L. Engel,[1] Xiao Zhang,[2] Mingming Wu,[2] Yan Wang,[2,3] Jose Espejo Valle-Inclán,[4] Qing Hu,[1] Kidist S. Woldehawariat,[1] Mathijs A. Sanders,[5,6] Agata Smogorzewska,[7] Jin Chen,[8,11,12] Isidro Cortés-Ciriano,[4] Roger S. Lo,[2,3,9] and Peter Ly[1,10,11,13,*]

[1]Department of Pathology, University of Texas Southwestern Medical Center, Dallas, TX 75390, USA
[2]Division of Dermatology, Department of Medicine, David Geffen School of Medicine, University of California, Los Angeles, Los Angeles, CA 90095, USA
[3]Department of Molecular and Medical Pharmacology, David Geffen School of Medicine, University of California, Los Angeles, Los Angeles, CA 90095, USA
[4]European Molecular Biology Laboratory, European Bioinformatics Institute, Wellcome Genome Campus, Hinxton, UK
[5]Cancer, Ageing and Somatic Mutation Programme, Wellcome Sanger Institute, Hinxton CB10 1SD, UK
[6]Department of Hematology, Erasmus MC Cancer Institute, Rotterdam 3015 GD, the Netherlands
[7]Laboratory of Genome Maintenance, Rockefeller University, New York, NY 10065, USA
[8]Cecil H. and Ida Green Center for Reproductive Biology Sciences, University of Texas Southwestern Medical Center, Dallas, TX 75390, USA
[9]Jonsson Comprehensive Cancer Center, David Geffen School of Medicine, University of California, Los Angeles, Los Angeles, CA 90095, USA
[10]Department of Cell Biology, University of Texas Southwestern Medical Center, Dallas, TX 75390, USA
[11]Harold C. Simmons Comprehensive Cancer Center, University of Texas Southwestern Medical Center, Dallas, TX 75390, USA
[12]Present address: Altos Labs, Bay Area Institute of Science, Redwood City, CA 94403, USA
[13]Lead contact
*Correspondence: peter.ly@utsouthwestern.edu
https://doi.org/10.1016/j.cell.2024.08.001

SUMMARY

Chromothripsis describes the catastrophic shattering of mis-segregated chromosomes trapped within micronuclei. Although micronuclei accumulate DNA double-strand breaks and replication defects throughout interphase, how chromosomes undergo shattering remains unresolved. Using CRISPR-Cas9 screens, we identify a non-canonical role of the Fanconi anemia (FA) pathway as a driver of chromothripsis. Inactivation of the FA pathway suppresses chromosome shattering during mitosis without impacting interphase-associated defects within micronuclei. Mono-ubiquitination of FANCI-FANCD2 by the FA core complex promotes its mitotic engagement with under-replicated micronuclear chromosomes. The structure-selective SLX4-XPF-ERCC1 endonuclease subsequently induces large-scale nucleolytic cleavage of persistent DNA replication intermediates, which stimulates POLD3-dependent mitotic DNA synthesis to prime shattered fragments for reassembly in the ensuing cell cycle. Notably, FA-pathway-induced chromothripsis generates complex genomic rearrangements and extrachromosomal DNA that confer acquired resistance to anti-cancer therapies. Our findings demonstrate how pathological activation of a central DNA repair mechanism paradoxically triggers cancer genome evolution through chromothripsis.

INTRODUCTION

Cancer genomes frequently harbor chromosomal abnormalities arising through punctuated episodes of genomic instability. This is exemplified by chromothripsis, which describes the catastrophic shattering and haphazard reassembly of individual chromosomes,[1] a process that scars one-third of tumors with complex localized genome rearrangements.[2,3] Chromothripsis is driven by mitotic errors that encapsulate mis-segregated chromosomes within abnormal extranuclear structures called micronuclei.[4–8] Dicentric chromosomes pulled in opposing directions by the mitotic spindle can also generate stretched chromatin bridges that persist into interphase, which fragment[9] or resolve into micronuclei-like nuclear structures.[10,11] Micronuclei harbor dysfunctional nuclear envelopes whose abrupt rupture during interphase disrupts nucleocytoplasmic compartmentalization,[12,13] rendering the underlying chromosome vulnerable to DNA double-strand breaks (DSBs) and/or DNA replication defects.[4,5] Several sources of interphase DNA damage have been identified,

including attack by the cytosolic exonuclease TREX1[14] and hyperactive base excision repair (BER) of RNA-DNA hybrids generated by terminated transcription.[15]

Whole chromosomes or chromosome arms isolated within micronuclei are susceptible to catastrophic shattering into tens to hundreds of fragments, which can be observed on metaphase spreads as highly pulverized chromosomes.[4,6] During the transition into mitosis, micronuclear chromosomes experience an additional burst of DNA damage that is accompanied by mitotic DNA synthesis,[10] a process termed MiDAS.[16,17] Fragments of the shattered chromosome re-incorporate into daughter cell nuclei at mitotic exit[4,18,19] and are subjected to error-prone DNA repair through non-homologous end joining (NHEJ) throughout the ensuing cell cycle.[6,20] This mutational cascade generates a broad spectrum of simple and complex genomic rearrangements, including extrachromosomal DNA (ecDNA) elements (or double minute chromosomes) from the ligation of chromothriptic fragments into a circular amplicon[5,7]. ecDNAs are associated with poor cancer prognosis and resistance to diverse clinical therapies.[11,21–23] Despite this knowledge, the molecular pathways that induce chromosome shattering remain incompletely understood.

We previously developed an inducible and chromosome-specific micronucleus system—termed CEN-SELECT—that enables the stepwise mechanisms of chromothripsis to be reconstructed in genome-edited human DLD-1 cells.[6,7] Induction with doxycycline and auxin (DOX/IAA) replaces the centromeric histone H3 variant CENP-A with a mutant that inactivates the centromere of the Y chromosome harboring a neomycin-resistance gene (*neoR*).[6,7] Centromere inactivation triggers the mis-segregation of the Y chromosome into micronuclei, which then undergo catastrophic shattering and rearrangements within a few cell cycles. Selection for the maintenance of genetically heritable derivative Y chromosomes with G418 couples the consequences of chromosome segregation errors and micronuclei formation to cell viability. In this study, we leveraged this platform to conduct pooled CRISPR-Cas9 screens to discover genetic pathways contributing to the biogenesis of chromothripsis from micronuclei. These efforts unexpectedly identified the Fanconi anemia (FA) pathway as an essential component driving chromothripsis.

The FA pathway is best characterized in DNA interstrand crosslink repair.[24] The FA core complex functions as an E3 ubiquitin ligase to mono-ubiquitinate the FANCI-FANCD2 heterodimer (known as the ID2 complex).[25,26] Once activated, FANCI-FANCD2 encircles the DNA[27,28] and recruits the SLX4 scaffold (also known as FANCP) along with one or more structure-specific endonuclease(s) to excise the lesion and initiate its repair.[29,30] The FA pathway further protects genome stability by acting at aberrant DNA replication structures.[31–34] For example, to prevent the formation of ultrafine bridges in anaphase, FANCD2 promotes the cleavage of DNA replication intermediates between sister chromatids persisting into mitosis, which can arise from difficult-to-replicate loci such as common fragile sites (CFSs).[35–38] Patients with germline mutations in FA genes exhibit congenital defects, bone marrow failure, anemia, and cancer predisposition, highlighting the critical genome maintenance function of the FA pathway.[39] Squamous cell carcinomas from FA patients harbor high levels of structural variants forming chains of complex rearrangements inter-connecting multiple chromosomes.[40] These are thought to arise in FA-deficient cells by end joining of inappropriately processed DSBs, which also contribute to radial chromosome formation.[40,41] Despite extensive structural variation, the genomic signatures of chromothripsis have not been detected in tumors from FA patients.[40]

Here we show that components of the FA pathway localize to under-replicated chromosomes from micronuclei during mitosis. Recruitment of the SLX4-XPF-ERCC1 endonuclease triggers the cleavage of DNA replication intermediates and induces widespread shattering of the micronucleated chromosome. POLD3-dependent MiDAS subsequently primes under-replicated fragments to become reassembled in the following cell cycle. Notably, inactivation of the FA pathway abolished mitotic chromosome shattering, blocking the formation of complex genomic rearrangements and ecDNAs harboring amplified drug-resistance genes. Thus, cancers can co-opt a genome-protective DNA repair pathway into a genome-destabilizing mechanism of instability and acquired therapy resistance. We propose that this mechanism of large-scale chromosome cleavage is analogous to, yet distinct from, the resolution of late-replicating CFS loci during mitosis, which normally functions to preserve genome integrity.

RESULTS

The FA pathway regulates chromothripsis without affecting interphase-associated micronuclei defects

To uncover genes that promote or suppress chromothripsis from micronuclei, we integrated the CEN-SELECT platform with pooled CRISPR-Cas9 screens targeting 365 genes involved in the DNA damage response (DDR)[42] (Figure 1A). This screen exploits the Y-encoded *neoR* marker to select for G418-resistant cells that maintain a heritable copy of the Y chromosome following its induction into micronuclei, the majority of which harbor a spectrum of complex rearrangements.[7] We reasoned that perturbing any step in the cascade of events resulting in chromothripsis (Figure S1A) would alter sensitivity to G418 selection, thereby providing a cell viability-based readout for pooled genetic screening. To do so, DLD-1 CEN-SELECT cells (hereafter referred to as DLD-1 cells) were transduced with the lentiviral DDR sgRNA library, selected with puromycin, and treated with or without DOX/IAA for 3 days to induce Y-chromosome-specific micronuclei and chromothripsis. Both conditions were then selected in parallel with G418, and as expected, most Y centromere-inactivated cells initially underwent G418-mediated cell death due to loss of the *neoR* marker followed by recovery of resistant cells.[7] Next-generation sequencing of sgRNA abundance following 14 and 25 days of selection yielded 26 DDR genes whose inactivation either significantly increased or decreased cell viability in G418 by at least 2-fold (Figure 1B; Table S1). There was a high degree of concordance between genes at both time points (Figure S1B), and several highly ranked hits were confirmed to alter G418 sensitivity using individual sgRNAs (Figures S1C and S1D).

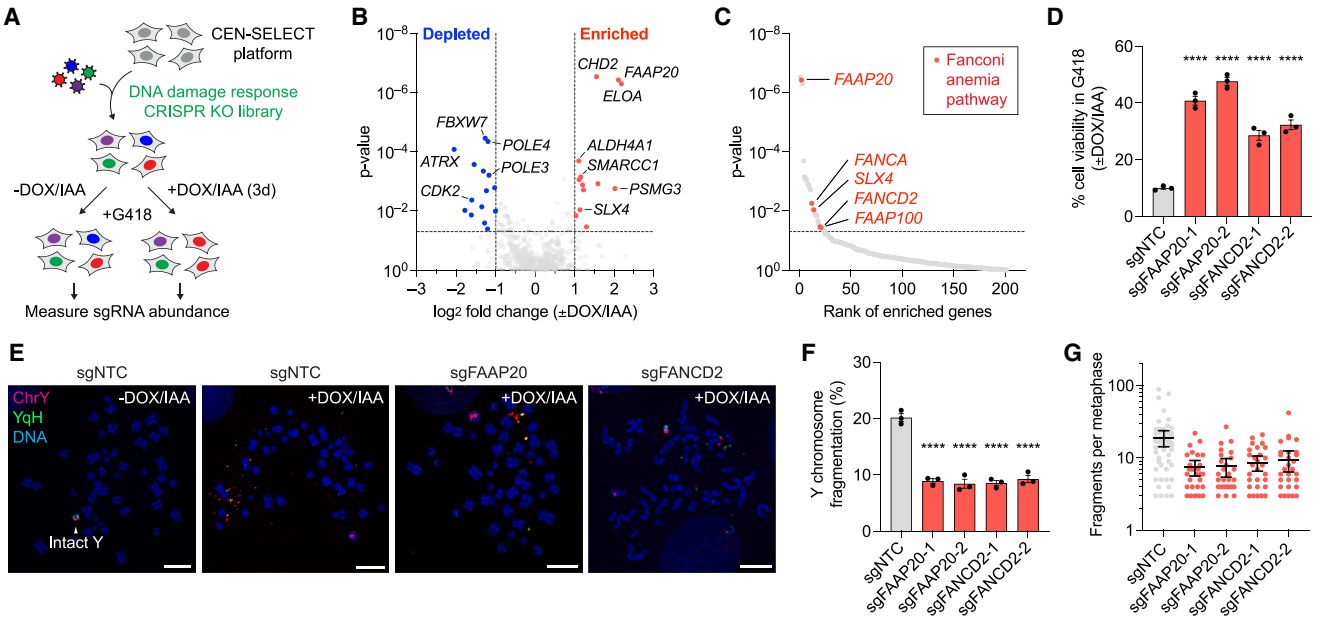

Figure 1. The FA pathway drives the catastrophic shattering of chromosomes from micronuclei during mitosis

(A) Schematic of pooled CRISPR-Cas9 knockout (KO) screen using a Y centromere inactivation and Y chromosome selection strategy to identify DNA damage response genes that promote or suppress chromothripsis.

(B) Volcano plot comparing the enrichment or depletion of genes in the DOX/IAA-induced condition versus untreated controls.

(C) Enriched genes (log_2 fold change > 0) ranked by p value. Statistical cutoff ($p \leq 0.05$) denoted by dotted line. Significant hits for genes involved in the Fanconi anemia (FA) pathway are indicated in red.

(D) CEN-SELECT growth assay in DLD-1 knockout (KO) FAAP20 and FANCD2 cells. Data represent mean ± SEM from $n = 3$ experiments.

(E) Representative metaphase spreads from FAAP20 and FANCD2 KO DLD-1 cells with intact or shattered Y chromosomes hybridized to DNA fluorescence *in situ* hybridization (FISH) probes. Scale bars, 10 μm.

(F) Y chromosome-shattering analysis by metaphase FISH from (E) following 72 h DOX/IAA induction. Data represent mean ± SEM from $n = 3$ experiments analyzing 275–314 metaphases.

(G) Number of fragments per metaphase containing a shattered Y chromosome from (E) and (F). Data represent mean ± 95% confidence interval (CI) from $n = 30$–54 metaphases pooled from 3 experiments.

Statistical analyses for (D) and (F) by ordinary one-way ANOVA test with multiple comparisons.

See also Figures S1 and S2 and Table S1.

Among the significantly enriched genes were multiple components of the FA pathway, which can be categorized into the FA core complex (*FANCA*, *FAAP20*, and *FAAP100*), the ID2 complex (*FANCD2*), or the tri-nuclease scaffold (*SLX4*) (Figures 1C, S1E, and S1F). Despite reported heterozygous mutations in *FANCA* and *BRCA2* (also known as *FANCD1*) in DepMap, parental DLD-1 cells maintained a functional FA pathway, as demonstrated by mono-ubiquitination of FANCD2 in response to the crosslinking agent mitomycin C (MMC) (upper band, Figure S1G). To validate the enrichment of FA genes from the screen, FAAP20 and FANCD2 knockout (KO) DLD-1 cell populations were generated using independent sgRNAs, which were expectedly hypersensitive to MMC, exhibited reduced mono-ubiquitination of FANCD2 upon loss of FAAP20, or were susceptible to MMC-induced radial chromosome formation (Figures S1H–S1J). When subjected to DOX/IAA-induced centromere inactivation, loss of FAAP20 or FANCD2 resulted in increased viability under G418 selection compared with wild-type (WT) controls (Figure 1D) without differences in spontaneous micronucleation at baseline (Figure S1K). Epistasis experiments showed no additive or synergistic effects in cells lacking both FAAP20 and FANCD2 (Figure S1L).

Next, we investigated how the FA pathway functions within the cascade of events from micronuclei to chromothripsis. Both FAAP20 and FANCD2 KO cells generated micronuclei at comparable levels after DOX/IAA induction (Figures S2A and S2B), and expression of a red fluorescent protein fused to a nuclear localization signal (RFP-NLS) reporter revealed similar frequencies in micronuclear envelope rupture (Figures S2A and S2C). Furthermore, there were no differences in the amount of DSBs in intact or ruptured micronuclei, as detected by immunostaining for phosphorylated histone H2AX (γH2AX) (Figures S2A and S2D). We then labeled cells with the nucleotide analog EdU to test whether FA-deficient cells exhibited defects in micronuclear DNA replication. Consistent with previous findings,[4,5,12] micronuclei displayed defective DNA replication compared with primary nuclei, and DNA synthesis was almost entirely terminated following NE rupture (Figures S2A and S2E), suggesting that the FA pathway does not contribute to the dysfunctional replication of micronuclear DNAs. Lastly, immunostaining for FANCD2 foci, a marker of FA pathway activation, revealed that FANCD2

does not accumulate to a detectable level within intact or ruptured micronuclei (Figures S2F–S2H), further excluding an interphase role of the FA pathway in driving chromothripsis.

Mitotic activation of the FA pathway triggers micronuclear chromosome shattering

Given the lack of overt differences in interphase micronuclei, we next examined metaphase spreads for Y chromosome shattering by DNA fluorescence *in situ* hybridization (FISH). Unexpectedly, in the mitosis following the induction of micronuclei, FA-deficient cells exhibited a measurable 2-fold reduction in the frequency of Y-chromosome-specific shattering (Figures 1E and 1F). The remaining metaphases with a shattered Y chromosome derived from FA-deficient cells contained fewer detectable FISH-labeled chromosome fragments compared with controls (Figure 1G). Whereas extensive mitotic chromosome shattering appears to be dependent on an intact FA pathway, we suspected that minimal chromosome-shattering events (i.e., those producing less than 10 visible fragments) may be caused by interphase-specific DNA damage in micronuclei. Indeed, CRISPR-mediated deletion of the BER DNA glycosylase MPG,[15] but not the cytosolic exonuclease TREX1,[14] suppressed both interphase DSBs in micronuclei (Figure S2J) and mitotic chromosome shattering (Figures S2K and S2L). However, in contrast to FAAP20- and FANCD2-deficient cells, the severity of chromosome shattering was similar between WT and MPG KO cells, with some metaphases yielding >100 fragments per event (Figure S2L). These data therefore uncouple the contributions of interphase DNA damage in micronuclei from an unanticipated FA-dependent mechanism that triggers extensive mitotic chromosome shattering.

Since the FA pathway can process CFSs during mitosis,[35,36] we used immunofluorescence combined with DNA FISH to visualize FANCD2 localization on intact or shattered Y chromosomes in mitosis, the latter marked by extensive γH2AX restricted to a confined region—a surrogate readout for chromothripsis in mitotic cells.[18,19] Indeed, FANCD2 co-localized with a significant fraction (~40%) of shattered mitotic Y chromosomes but not intact control chromosomes (Figures 2A and 2B). Inspection of cells at distinct stages of mitosis revealed that although FANCD2 recruitment is initially delayed during mitotic entry, it rapidly localizes to the micronucleated chromosome by prometaphase and remains associated with the fragments upon its re-incorporation into daughter cell nuclei as a micronucleus body (MN body) (Figures 2C and S3A). The initial delay in FANCD2 recruitment to micronucleated chromosomes appears distinct from aphidicolin (APH)-induced recruitment of FANCD2 to CFSs, which are visible as early as prophase (Figures S3B and S3C). Biallelic inactivation of *FANCD2* in two CRISPR-edited clones (*FANCD2*$^{-/-}$, Figures S3D and S3E) completely abolished immunofluorescent detection of FANCD2 and suppressed mitotic γH2AX-labeled Y chromosomes by about half (Figure 2D). Consistent with previous KO cell populations (Figures 1E and 1F), analysis of metaphase spreads derived from *FANCD2*$^{-/-}$ clones showed reductions in both the frequency and severity of shattered Y chromosomes (Figures 2E and 2F). These data indicate that FANCD2 recruitment to micronuclear chromosomes during mitosis is required for chromosome shattering.

The FA core complex activates the FA pathway by mono-ubiquitinating the FANCI-FANCD2 heterodimer on lysine residues 523 and 561, respectively.[25,26] As expected, KO of *FANCI*, components of the FA core complex (*FANCA* and *FANCL*), or the core complex anchoring factor (*FANCM*) reduced FANCD2 mono-ubiquitination following exposure to MMC (Figure S3F). Consistent with loss of FANCD2 mono-ubiquitination, loss of FANCM or FANCL was sufficient to inhibit FANCD2 recruitment during mitosis (Figure 2G), resulting in a corresponding reduction in γH2AX-labeled mitotic Y chromosomes (Figure 2H). In agreement, metaphases from cells lacking FANCI, FANCM, or members of the FA core complex exhibited reduced Y chromosome shattering (Figures 2I and 2J). Complementation of FANCD2-deficient cells with WT FANCD2 restored Y chromosome shattering, whereas a ubiquitination-resistant mutant (K561R) failed to rescue (Figures 2K and S3G). Altogether, FA-driven mitotic shattering of micronuclear chromosomes requires canonical activation of FANCI-FANCD2 through lysine 561 mono-ubiquitination of FANCD2 by the FA core complex.

The SLX4-XPF-ERCC1 endonuclease complex cleaves micronucleated chromosomes

Activated FANCI-FANCD2 promotes the recruitment of the nuclease scaffold SLX4 to interstrand crosslinks, which coordinates the activity of three distinct structure-specific endonucleases to cleave abnormal DNA lesions: MUS81-EME1, XPF-ERCC1, and SLX1.[43–45] These interactions form the SMX tri-nuclease complex that unhooks interstrand crosslinks,[30,43] resolves Holliday junctions inappropriately linking sister chromatids,[45] and processes topoisomerase intermediates.[46] These mechanisms also act in conjunction with the cytosolic GEN1 endonuclease, which largely functions during mitosis.[47,48]

To visualize whether SLX4 is recruited to micronucleated chromosomes during mitosis, we induced micronuclei in DLD-1 cells expressing SLX4 fused to green fluorescent protein (SLX4-GFP). Live-cell imaging showed co-localization between SLX4-GFP with visibly shattered mitotic chromatin labeled with histone H2B-mCherry (Figure 3A). To determine whether SLX4-dependent nucleases and/or GEN1 participate in driving chromothripsis during mitosis, MUS81, XPF, SLX1, and GEN1 were depleted by RNA interference and assayed for Y chromosome shattering. Only depletion of the XPF endonuclease was sufficient to suppress chromosome shattering with a corresponding reduction in the number of fragments produced per event (Figures 3B, 3C, and S4A). This was further confirmed in CRISPR-mediated XPF KO cells, which exhibited reduced chromosome shattering without affecting interphase DNA damage in micronuclei (Figures 3D, 3E, S4B, and S4C) in a manner mirroring cells lacking FAAP20 or FANCD2 (Figures 1F and 1G). Mitotic chromosome shattering was similarly suppressed in *SLX4*$^{-/-}$ DLD-1 cells without reductions in interphase micronuclear γH2AX levels (Figures 3F, 3G, and S4D). Ectopic expression of full-length SLX4-GFP rescued Y chromosome shattering in *SLX4*$^{-/-}$ cells to levels comparable to controls, but not an XPF binding-deficient mutant of SLX4 with two alanine substitutions (L530A and W531A) in its MLR domain (Figures 3F and 3G). Interestingly, depletion of MUS81 increased the frequency and severity of

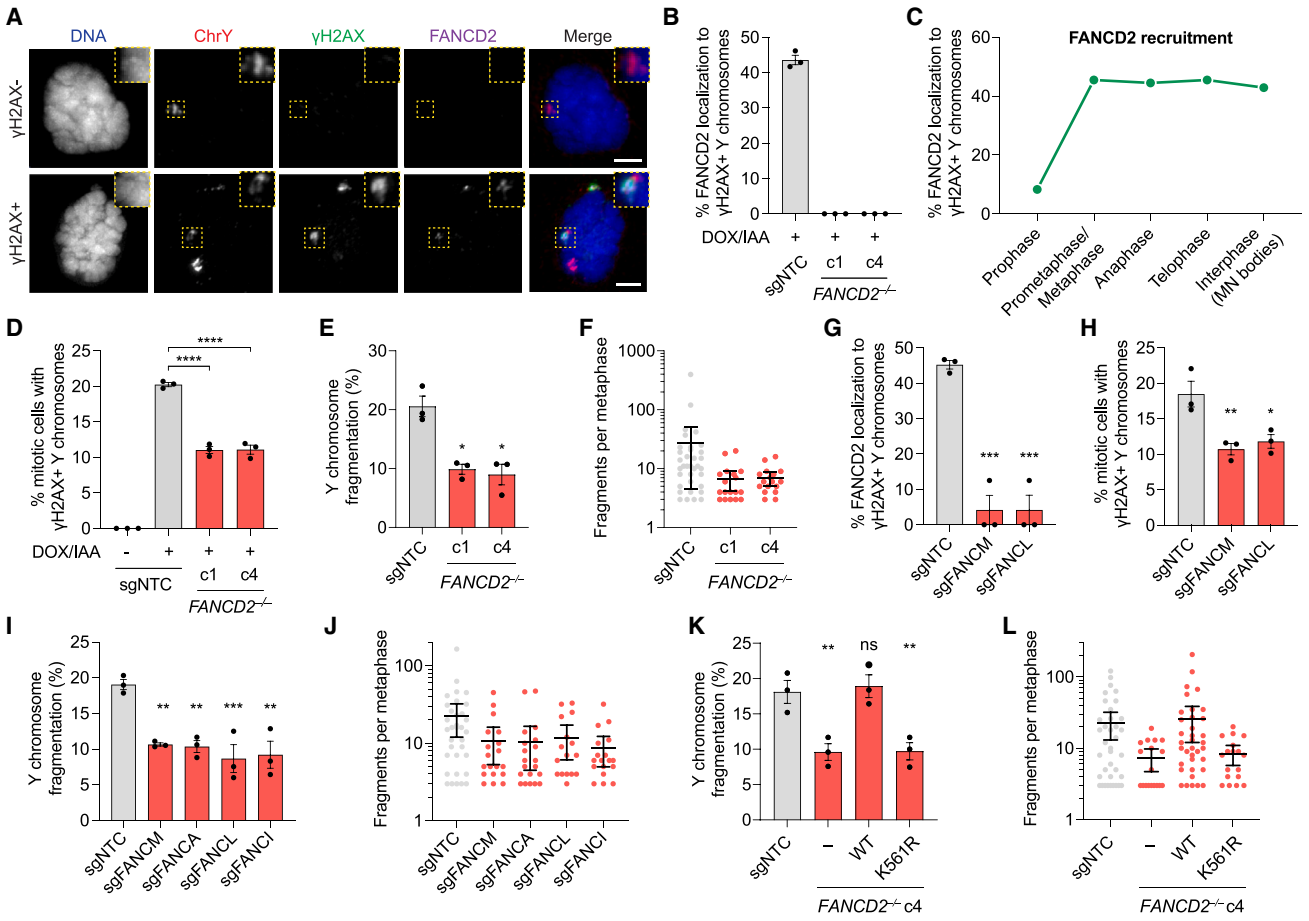

Figure 2. Mitotic localization of FANCD2 to micronuclear chromosomes requires canonical activation of the FA pathway

(A) Representative images of FANCD2 localization to shattered Y chromosomes in 72 h DOX/IAA-induced DLD-1 cells as detected by γH2AX and FANCD2 immunofluorescence and Y chromosome DNA FISH. Scale bars, 5 μm.

(B) FANCD2 localization to shattered Y chromosomes (marked by extensive γH2AX) from (A) in *FANCD2*$^{-/-}$ DLD-1 clones following 72 h DOX/IAA induction.

(C) FANCD2 localization to shattered Y chromosomes at the indicated stages of mitosis or interphase. Data represent mean from n = 9–44 cells pooled from 4 experiments. Example images shown in Figure S3A.

(D) Quantification of shattered Y chromosomes in 72 h DOX/IAA-treated DLD-1 cells in mitosis.

(E) Y chromosome-shattering analysis by metaphase FISH following 72 h DOX/IAA induction.

(F) Number of fragments per metaphase containing a shattered Y chromosome from (E). Data represent the mean ± 95% CI from n = 17–35 metaphases pooled from 3 experiments.

(G) FANCD2 localization to shattered Y chromosomes in FANCM and FANCL KO DLD-1 cells.

(H) Quantification of shattered Y chromosomes in FANCM and FANCL KO DLD-1 cells following 72 h DOX/IAA induction.

(I) Y chromosome-shattering analysis by metaphase FISH following 72 h DOX/IAA induction.

(J) Number of fragments per metaphase containing a shattered Y chromosome from (I). Data represent the mean ± 95% CI from n = 18–34 metaphases pooled from 3 experiments.

(K) Y chromosome-shattering analysis by metaphase FISH following 72 h DOX/IAA induction.

(L) Number of fragments per metaphase containing a shattered Y chromosome from (K). Data represent the mean ± 95% CI from n = 18–37 metaphases pooled from 3 experiments.

Data in (B), (D), (E), (G)–(I), and (K) represent mean ± SEM of n = 3 experiments analyzing (B) 308–321 mitotic cells, (D) 304–321 mitotic cells, (E) 289–311 metaphases, (G) 302–311 cells, (H) 302–311 mitotic cells, (I) 199–233 metaphases, and (K) 279–296 metaphases. Statistical analyses for (D), (E), (G)–(I), and (K) by ordinary one-way ANOVA test with multiple comparisons.

See also Figure S3.

shattered chromosomes (Figures 3B and 3C), consistent with slightly elevated spontaneous chromosome shattering upon MUS81 loss.[49]

To evaluate these pathways in a complementary experimental system, we sought to identify shattered chromosomes in diploid human RPE-1 cells following chemical inhibition of the Mps1 spindle assembly checkpoint kinase, which induced a ~37-fold increase in micronuclei containing random chromosomes (24.9% versus 0.68% of cells). Using multiplex-FISH to reconstruct individual karyotypes from 607 metaphases (Figure 3H),

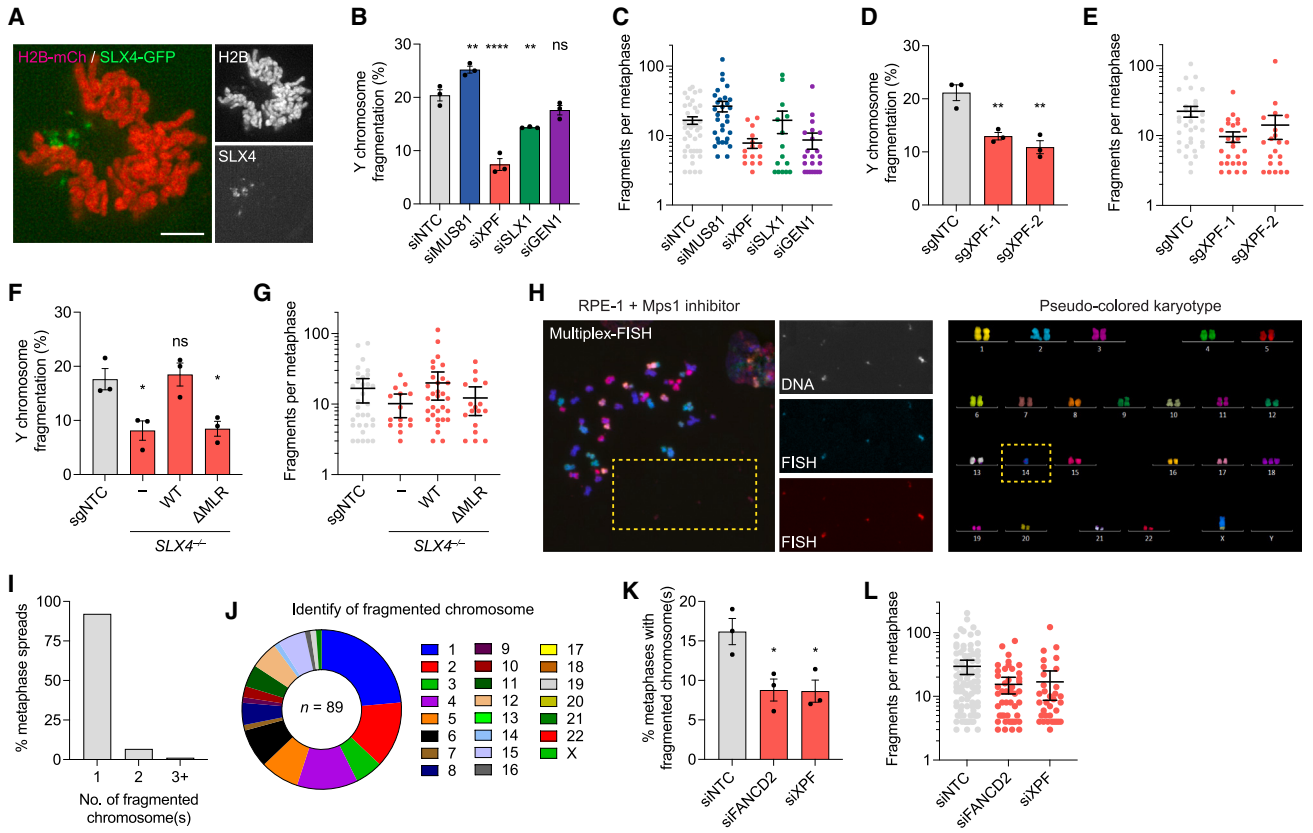

Figure 3. Nucleolytic cleavage of micronuclear chromosomes by the structure-specific SLX4-XPF-ERCC1 endonuclease complex

(A) Representative image of SLX4-GFP localizing to a shattered chromosome during mitosis following 72 h DOX/IAA induction. Scale bars, 5 μm.

(B) Y chromosome-shattering analysis by metaphase FISH following DOX/IAA induction for 72 h.

(C) Number of fragments per metaphase containing a shattered Y chromosome from (B). Data represent the mean ± 95% CI from n = 15–42 metaphases pooled from 3 experiments.

(D) Y chromosome-shattering analysis by metaphase FISH following 72 h DOX/IAA induction.

(E) Number of fragments per metaphase containing a shattered Y chromosome from (D). Data represent the mean ± 95% CI from n = 21–34 metaphases pooled from 3 experiments.

(F) Y chromosome-shattering analysis by metaphase FISH following 72 h DOX/IAA induction from an *SLX4*$^{-/-}$ clone complemented with WT or MLR-mutated SLX4.

(G) Number of fragments per metaphase containing a shattered Y chromosome from (F). Data represent the mean ± 95% CI from n = 17–32 metaphases pooled from 3 experiments.

(H) Metaphase spread from RPE-1 cell treated with an Mps1 inhibitor for 24 h and labeled by multiplex-FISH (left), and boxed region indicates a shattered chromosome 14. Reconstructed karyotype with pseudo-colored chromosomes exhibiting loss of chromosome 14 is shown on the right.

(I) Quantification of the number of shattered chromosomes identified per metaphase spread in RPE-1 cells following treatment with an Mps1 inhibitor for 24 h. Data represent n = 89 metaphases with at least one shattered chromosome. A total of 607 metaphases pooled from 3 experiments were analyzed.

(J) Identity of shattered chromosomes from (H) and (I).

(K) Shattered chromosomes in RPE-1 cells by multiplex-FISH following siRNA-mediated depletion of FANCD2 or XPF and treatment with an Mps1 inhibitor for 24 h.

(L) Number of fragments per metaphase containing a shattered chromosome from (K). Data represent the mean ± 95% CI from n = 34–90 metaphases pooled from 3 experiments.

Data in (B), (D), (F), and (K) represent mean ± SEM of n = 3 experiments analyzing (B) 328–365 metaphases; (D) 296–310 metaphases; (F) 296–311 metaphases; (K) 401–607 metaphases. Statistical analyses for (B), (D), (F), and (K) by ordinary one-way ANOVA test with multiple comparisons.

See also Figure S4.

we identified chromosome-shattering events affecting 17 out of 22 human autosomes, the majority (~92%) of which impacted a single chromosome per cell (Figures 3I and 3J). In agreement with results from DLD-1 cells, depletion of FANCD2 or XPF suppressed chromosome-shattering frequency by ~53% with corresponding reductions in fragmentation severity (Figures 3K, 3L, and S4E). These data demonstrate that FA-driven chromothripsis can be generalizable across experimental models and chromosomes throughout the human genome.

To further exclude the possibility of cell-type-specific preferences for XPF-ERCC1 in DLD-1 cells, we evaluated the activity of FANCD2, SLX4, and its associated endonucleases in two

related yet distinct contexts: mitotic CFS expression triggered by APH-induced polymerase stalling[50] and the pulverization of actively replicating genomes induced by WEE1 inhibition.[51] As expected, both FANCD2 and SLX4 contributed to APH-induced MiDAS at chromosome gaps/breaks (Figures S4F and S4G), as well as all four endonucleases (Figure S4H). By contrast, S-phase cells exposed to a WEE1 inhibitor induced genome-scale pulverization that was dependent on SLX4, MUS81, and GEN1 (Figures S4I–S4K), indicative of context-specific selectivity in nuclease choice. We propose that the FA pathway promotes the cleavage of chromosomes from micronuclei during mitosis through recruitment of the SLX4-XPF-ERCC1 endonuclease complex in a process analogous to mitotic CFS expression.

Shattered mitotic chromosomes originate from under-replicated DNA from the prior interphase

We hypothesized that shattered chromosomes undergoing FA-mediated processing are derived from under-replicated micronuclear chromosomes from the prior interphase. To test this, DLD-1 cells with micronuclei were arrested in G1 with the Cdk4/6 inhibitor palbociclib, released into S-phase for 16 h in EdU, and examined by metaphase FISH. Intact Y chromosomes fully incorporated EdU similarly to non-micronucleated control chromosomes, whereas EdU labeling was sharply reduced in fragments derived from shattered Y chromosomes (Figures 4A and 4B). Inspection of interphase DLD-1 cells at the corresponding time point confirmed that, although most nuclei displayed pan-nuclear EdU staining indicative of successful passage through S-phase, most ruptured micronuclei (lacking RFP-NLS) exhibited trace or undetectable amounts of EdU (as denoted by a low micronucleus/primary nucleus [MN/PN] ratio; Figures S5A and S5B), in agreement with prior studies.[4,5,12] As shown in Figure S2E, such interphase replication defects are independent of the FA pathway. In RPE-1 cells treated with an Mps1 inhibitor and labeled with EdU for 24 h, FANCD2 localized to ~75% of shattered chromosomes during mitosis, nearly all of which failed to incorporate EdU (Figures S5C–S5E), indicative of the cleavage of incomplete DNA replication intermediates.

Most ruptured micronuclei exhibited DNA replication defects, although this did not always correspond with the acquisition of DNA damage (Figure S5B). To determine whether FA-induced chromosome shattering is dependent on DNA replication defects driven by micronuclear envelope rupture, we modulated the levels of lamin B2, a component of the nuclear lamina.[12] Lamin B2 overexpression did not alter DOX/IAA-induced micronuclei formation but restored the stability of its nuclear envelope, as determined by retention of the retinoblastoma protein (Rb) as a marker for rupture[12] (Figures S5F–S5I). Suppression of micronuclear envelope rupture mitigated both interphase DNA damage and mitotic DNA damage driven by DNA replication defects, thereby reducing the frequency of chromosome shattering (Figures S5J and S5K) but not the number of fragments per event (Figure S5L). FANCD2 recruitment to Y chromosomes was similarly suppressed in lamin B2-overexpressing cells (Figure S5M). Thus, micronuclear envelope rupture initiates micronuclei-associated defects that ultimately shatter the entrapped chromosome.

Nucleolytic shattering of micronuclear chromosomes is coupled to mitotic DNA synthesis

Micronucleated chromosomes undergo a burst of DNA synthesis during mitosis,[10] which resembles MiDAS at late-replicating CFSs.[16] To determine whether the FA pathway is associated with micronuclei-associated MiDAS, DLD-1 cells with micronuclei were briefly pulsed with EdU for 30 min prior to immunostaining for FANCD2. ~10% of mitotic cells displayed Y-chromosome-specific incorporation of EdU, the majority (~80%) of which co-localized with FANCD2 (Figures S6A and S6B). These findings were extended to RPE-1 cells harboring micronuclei induced by inhibition of the Mps1 mitotic kinase or microtubule polymerization with nocodazole (Figures S6C and S6D) and HeLa and DLD-1 cells treated with an Mps1 inhibitor (Figure S6E). The observed EdU signal often co-localized with PCNA (Figure S6F), a DNA clamp essential for DNA replication. Inspection of metaphase spreads revealed that EdU-incorporated chromosomes were susceptible to the more severe form of shattering, producing a median of 27 EdU-positive fragments per event, whereas EdU-negative shattered chromosomes harbored a median of 5 fragments (Figures 4C and 4D). Accordingly, the majority of chromosome-shattering events incorporating EdU during mitosis was abolished in cells lacking FANCD2 (Figure 4E), suggesting that MiDAS is dependent on FA-induced cleavage of micronuclear chromosomes.

Micronuclei-like nuclear protrusions from chromatin bridges are similarly processed by the FA pathway

Chromatin bridges from dicentric chromosomes can resolve into micronuclei and/or micronuclei-like nuclear protrusions, which also undergo a burst of DNA synthesis during mitosis.[10] To evaluate whether the FA pathway promotes chromothripsis from chromatin bridges, we visualized the localization of FANCD2 in asynchronous RPE-1 cells expressing a DOX-inducible dominant-negative allele of TRF2 (TRF2-DN) to trigger telomere dysfunction and dicentric chromosome fusions.[9] FANCD2 was undetectable on damaged yet intact chromatin bridges during interphase (Figures S6G and S6H), and inactivation of the FA pathway did not affect the frequency of bridge breakage (Figure S6I). In agreement with a prior study,[10] broken chromatin bridges frequently formed γH2AX-positive micronuclei-like nuclear protrusions during interphase (Figure S6J). Strikingly, following a brief 30 min pulse with EdU, approximately two-thirds of non-S-phase cells harbored EdU-incorporated nuclear protrusions that accumulated FANCD2 foci (Figures S6J and S6K), often persisting into mitosis (Figure S6L). DNA synthesis on nuclear protrusions was dependent on the FA pathway as depletion of FANCD2 or XPF (Figure S6M) abolished EdU incorporation during both interphase and mitosis (Figures S6N and S6O). Induction of chromatin bridges also triggered the appearance of DAPI-stained mitotic fragments in one-third of metaphases (Figure 4F), indicative of TREX1- and/or actomyosin force-mediated chromosome shattering during or shortly after bridge resolution.[9,10,52] Regardless of how the chromatin bridge was broken, extensively shattered chromosomes incorporated EdU and underwent MiDAS in a FANCD2-dependent manner, whereas EdU was undetectable in cells with minimal chromosome breakage (Figures 4F–4H and S6M). These findings indicate that the FA pathway promotes chromothripsis on resolved

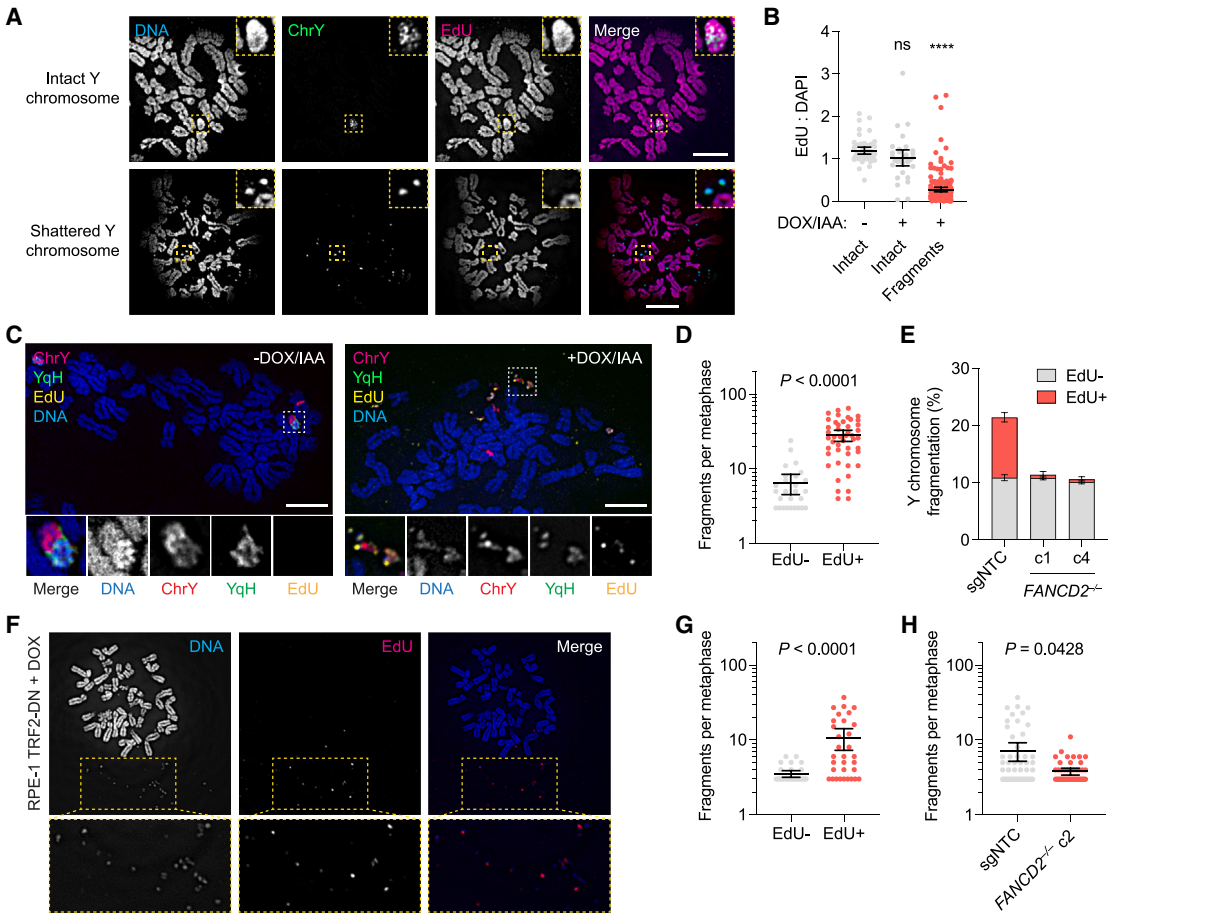

Figure 4. Cleavage of under-replicated chromosomes from micronuclei by the FA pathway is coupled to mitotic DNA synthesis

(A) Representative images of metaphase spreads from DLD-1 cells labeled with EdU for 16 h prior to fixation and DNA FISH. Scale bars, 5 μm.

(B) Quantification of EdU to DAPI intensity on intact or shattered Y chromosomes from (A). Data are from a representative experiment repeated 3 times from $n = 50$ (−DOX/IAA) and 33 (+DOX/IAA) intact chromosomes or $n = 182$ fragments pooled from 9 metaphase spreads with a shattered Y chromosome; statistical analysis by ordinary one-way ANOVA test with multiple comparisons.

(C) Metaphase spreads from 72 h DOX/IAA-treated DLD-1 cells pulsed with EdU for 30 min prior to fixation. Scale bars, 5 μm.

(D) Number of fragments per metaphase containing a shattered Y chromosome from (C) with and without EdU incorporation. Data represent the number of fragments from $n = 27$ and 44 metaphases pooled from 3 experiments.

(E) Y chromosome-shattering analysis by metaphase FISH following 72 h induction with DOX/IAA and 30 min pulse with EdU in DLD-1 control cells or *FANCD2*$^{-/-}$ clones. Data represent mean ± SEM from $n = 3$ experiments analyzing 274–301 metaphases.

(F) Example of metaphase spread with a shattered chromosome from doxycycline-induced RPE-1 cells expressing a dominant-negative TRF2 mutant (TRF2-DN) pulsed with EdU for 30 min prior to fixation.

(G) Number of fragments per metaphase containing a shattered Y chromosome from (F) with and without EdU incorporation. Data represent the number of fragments from $n = 29$ and 32 metaphases pooled from 3 experiments.

(H) Number of fragments per metaphase containing a shattered chromosome from (F) and (G). Data represent the number of fragments from $n = 63$ and 56 metaphases pooled from 3 experiments.

Statistical analyses for (D), (G), and (H) by Mann-Whitney test.

See also Figures S5 and S6.

chromatin bridges and micronuclei-like nuclear structures during interphase that can persist into mitosis.

Mitotic DNA synthesis primes cleaved replication intermediates for reassembly in the following cell cycle

Following mitotic chromosome shattering, chromosome fragments are asymmetrically inherited by one or both daughter cell(s)[5,18,19] and undergo nuclear re-incorporation as interphase MN bodies, which act as hubs for engaging the DDR.[20,53] Inspection of chromosome fragments on metaphase spreads revealed strong co-localization between sites of MiDAS and RPA32, a single-stranded DNA (ssDNA) binding protein (Figure 5A). Similarly, in Mps1 inhibitor-treated RPE-1 cells, RPA32 co-localized with MiDAS foci on shattered mitotic chromosomes in a FANCD2-dependent manner (Figures 5B and 5C). The presence of ssDNA at RPA32-marked sites was further confirmed by

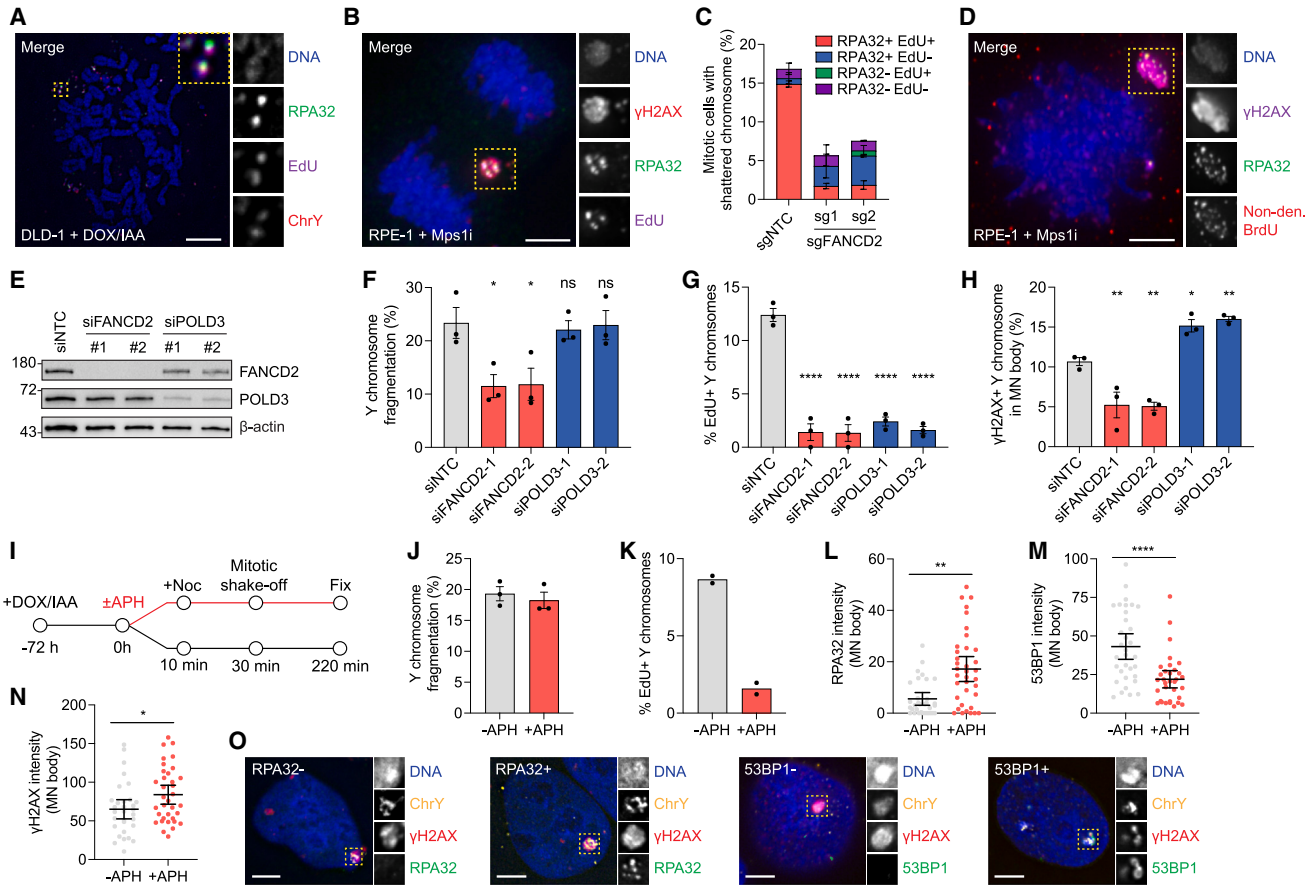

Figure 5. POLD3-dependent mitotic DNA synthesis primes cleaved replication intermediates for repair in the following cell cycle

(A) Example of metaphase spread from DLD-1 cell showing co-localization between RPA32 and EdU on Y chromosome fragments following 72 h DOX/IAA induction and 30 min pulse with EdU prior to fixation. Scale bars, 10 μm.

(B) Co-localization of RPA32 and EdU on shattered chromosome in RPE-1 cells treated with an Mps1 inhibitor for 24 h and 30 min pulse with EdU prior to fixation. Scale bars, 5 μm.

(C) Quantification of RPA32 and MiDAS on shattered chromosomes from (B). Data represent mean ± SEM of *n* = 3 experiments analyzing *n* = 221–248 mitotic cells.

(D) Co-localization of BrdU (non-denaturing) and RPA32 on a shattered chromosome in RPE-1 cells treated with an Mps1 inhibitor for 24 h. Scale bars, 5 μm.

(E) Immunoblot confirming depletion of FANCD2 or POLD3 in DLD-1 cells 72 h post-transfection.

(F) Y chromosome-shattering analysis by metaphase FISH following 72 h induction with DOX/IAA induction.

(G) EdU-incorporated Y chromosomes following 72 h DOX/IAA induction and pulse with EdU for 30 min prior to fixation.

(H) Quantification of re-integrated shattered Y chromosomes following 96 h DOX/IAA in DLD-1 cells.

(I) Experimental schematic for (J)–(O).

(J) Y chromosome-shattering analysis by metaphase FISH following DOX/IAA induction for 72 h and aphidicolin (APH) treatment for 40 min before collection of metaphase spreads.

(K) EdU-incorporated Y chromosomes following 72 h induction with DOX/IAA treated with or without APH for 10 min prior to addition of EdU for 30 min prior to fixation. Data represent mean of *n* = 2 experiments analyzing 197 and 209 mitotic cells.

(L–N) Intensities of RPA32 (L), 53BP1 (M), and γH2AX (N) in MN bodies identified by γH2AX immunostaining.

(O) Representative examples of Y chromosome-containing MN bodies induced by DOX/IAA for 96 h and immunostained for RPA32 or 53BP1. Scale bars, 5 μm. Data in (F)–(H) and (J) represent mean ± SEM of *n* = 3 experiments analyzing (F) 287–304 metaphases, (G) 296–312 mitotic cells, (H) 257–397 interphase cells, and (J) 314 and 285 metaphases. Data in (L)–(N) represent mean ± 95% CI of *n* = (L) 32 and 36 interphase cells, (M) 39 and 44 interphase cells, and (N) 31 and 35 interphase cells pooled from 3 experiments. Statistical analyses by ordinary one-way ANOVA test with multiple comparisons for (F)–(H) and by Mann-Whitney test for (L) and (M).

the detection of incorporated bromodeoxyuridine (BrdU) under non-denaturing conditions (Figure 5D). Chromosome fragments with ssDNA-containing ends are likely incompatible for repair by NHEJ, suggesting that further processing may be required for its reassembly in the following cell cycle.

To investigate the function of MiDAS in fragment reassembly, we first depleted POLD3, a subunit of DNA polymerase delta that is critical for MiDAS at late-replicating CFSs.[16] Unlike cells lacking FANCD2, depletion of POLD3 did not impact mitotic chromosome shattering but instead suppressed MiDAS

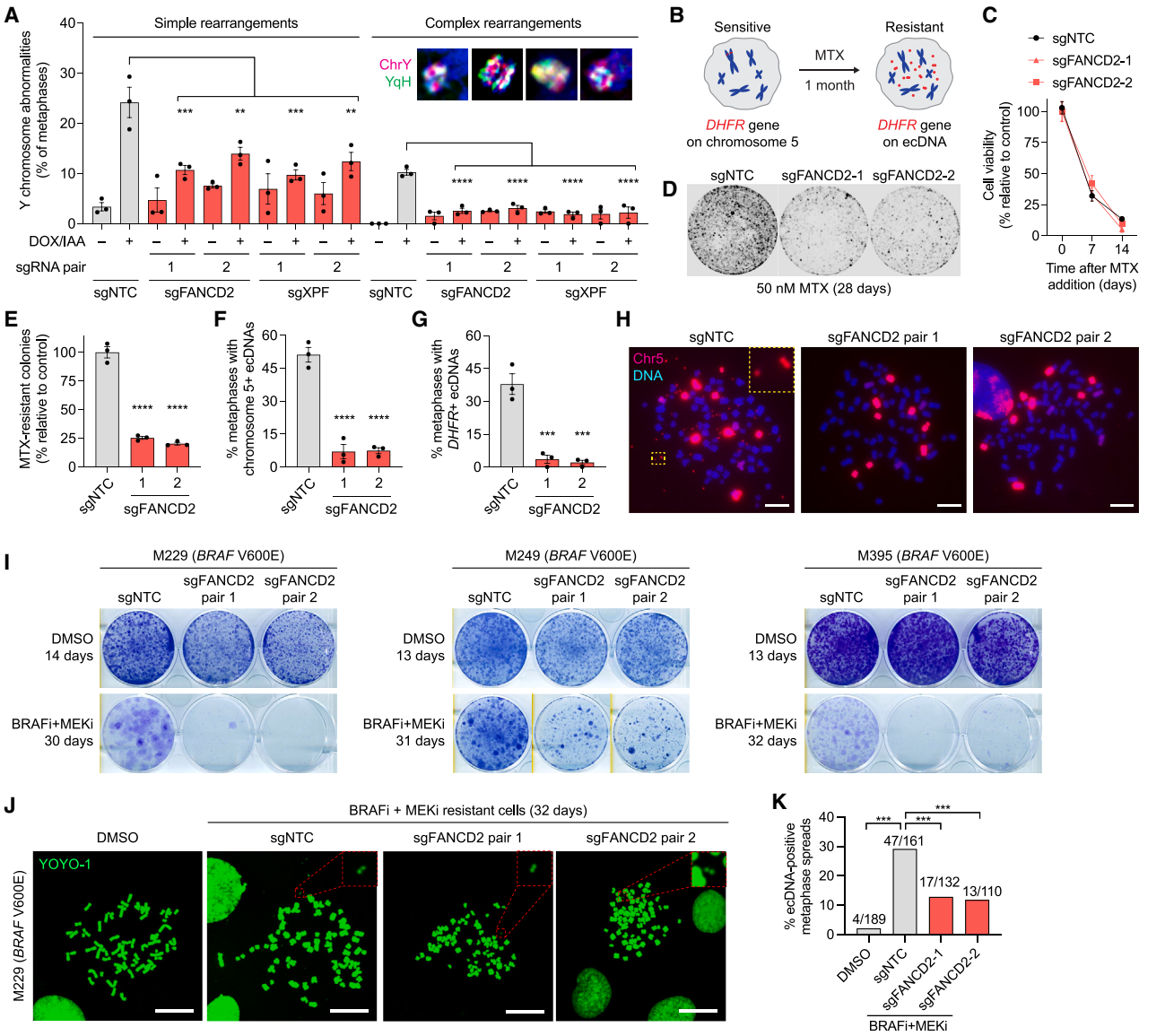

Figure 6. FA-pathway-induced chromothripsis generates complex genomic rearrangements and extrachromosomal DNAs that confer resistance to anti-cancer therapies

(A) Quantification of Y chromosome rearrangements following DOX/IAA induction and G418 selection. Data represent mean ± SEM of $n = 3$ experiments analyzing 111–340 metaphases; statistical analysis by ordinary one-way ANOVA test with multiple comparisons. Additional examples of complex Y rearrangements are shown in Figure S7B.

(B) Schematic of chromothripsis-mediated resistance to methotrexate (MTX) through *DHFR* amplification on ecDNAs.

(C) Cell viability of FANCD2 KO HeLa cells treated with 50 nM MTX for up to 2 weeks. Data represent mean ± SEM from $n = 3$ experiments performed in triplicate.

(D) Representative crystal violet staining of 2×10^6 FANCD2 KO HeLa cells treated with MTX for 28 days.

(E) Frequency of MTX-resistant colonies from (D). Data represent mean ± SEM from $n = 3$ experiments.

(F and G) Quantification of detectable ecDNA structures as visualized by metaphase FISH for chromosome 5 (F) or the *DHFR* locus (G) from resistant cells obtained from (D) and (E). Data represent mean ± SEM of $n = 3$ experiments analyzing 130–135 metaphases using chromosome 5 probes or 90–110 metaphases using *DHFR* probes; statistical analyses in (E)–(G) by ordinary one-way ANOVA test with multiple comparisons. Example images using *DHFR* FISH probes shown in Figure S7I.

(H) Representative metaphase FISH images of MTX-resistant cells hybridized to chromosome 5 paint probes. Magnified inset shows ecDNA foci. Scale bars, 10 μm.

(I) Long-term clonogenic growth assays for the indicated *BRAF*-mutant melanoma lines treated with DMSO or combination BRAFi + MEKi for the indicated days. Experiments were repeated three times for M229 and M395 and twice for M249.

(J) Representative images of metaphase spreads derived from M229 cells treated with DMSO or BRAFi + MEKi for ~1 month and stained with YOYO-1 to detect ecDNAs. Scale bars, 20 μm.

(legend continued on next page)

(Figures 5E–5G), suggesting POLD3 functions downstream of nucleolytic cleavage of the micronucleated chromosome. Knockdown of FANCD2 suppressed the formation of MN bodies, while loss of POLD3 conversely led to an accumulation of MN bodies (Figure 5H), one-third of which stained positive for RPA32 (31/85 MN bodies). As a complementary approach, MiDAS was inhibited by exposure to high-dose APH during mitosis, and MN bodies were inspected in G1-phase cells following release from nocodazole-induced mitotic arrest (Figure 5I). Addition of APH did not impact chromosome shattering but suppressed MiDAS, further supporting that MiDAS is initiated by chromosome breakage (Figures 5J and 5K). In control cells, ssDNA fragments were successfully converted to double-stranded DNA and recruited the NHEJ-promoting factor 53BP1; however, suppression of MiDAS resulted in persistent ssDNA at sites of DNA damage within MN bodies that impaired engagement by 53BP1(Figures 5L–5O). We propose that MiDAS facilitates the conversion of cleaved replication intermediates into blunt-ended DSBs that are ligatable by the error-prone NHEJ pathway.

FA-pathway-induced chromosome shattering is required for generating complex genomic rearrangements and ecDNAs

Chromothripsis from micronuclei and chromatin bridges gives rise to a continuum of simple and complex genomic rearrangements.[7,9,10,20,52] To determine whether the FA pathway contributes to these rearrangements, we targeted FANCD2 or XPF using pairs of sgRNAs that were each coupled to individual selection markers, enabling efficient DLD-1 KO populations to be generated without single-cell cloning (Figure S7A). Following centromere inactivation and selection with G418, metaphase spreads were analyzed for a spectrum of Y-chromosome-specific rearrangements using a dual-colored FISH approach exploiting two chromosome paint probes that do not normally overlap (Figure S7B). As previously validated, this cytogenetics-based strategy can reliably call complex rearrangements arising through chromothripsis as compared with whole-genome sequencing.[7] Although loss of the FA pathway slightly increased the basal level of genomic rearrangements consistent with its genome-maintenance function, FA-deficient cells harbored fewer overall simple rearrangements composed of translocations, fusions, and arm-level deletions upon micronuclei induction (Figure 6A), which presumably arise from micronuclei with less extensive DNA replication defects (Figures 4A–4E). Most notably, in cells lacking FANCD2 or XPF, there were marked reductions (~80%) in complex rearrangements that are detectable by the merging of the two FISH probes (Figure 6A). Depletion of FANCD2 or POLD3 was also sufficient to reduce the formation of complex rearrangements (Figures S7C and S7D), whereas inhibiting MPG-dependent interphase DNA damage in micronuclei had no effect (Figures S7E and S7F). Thus, FA-induced mitotic chromosome shattering robustly generates complex genomic rearrangements from micronuclei.

In addition to genomic rearrangements, chromothripsis underlies the generation of ecDNAs[5,7] that undergo positive selection in response to treatment with diverse anti-cancer therapeutics.[11,21–23,54,55] Mechanistically, one or more chromosome fragment(s) can ligate into a circular DNA structure for subsequent amplification.[7] To determine whether FA-induced chromothripsis can trigger ecDNA formation, we first leveraged an established system whereby long-term exposure to methotrexate (MTX)—a chemotherapeutic agent targeting dihydrofolate reductase (DHFR)—leads to chromothripsis-mediated amplification of ecDNAs containing the chromosome 5-encoded *DHFR* gene in emergent drug-resistant cells (Figure 6B).[11,56,57]

CRISPR-Cas9 editing was used to generate FANCD2 KO HeLa cells (Figure S7G), which proliferated similarly to WT controls (Figure S7H) and did not exhibit differences in sensitivity upon initial exposure to MTX (Figure 6C). However, after 28 days in MTX, resistant cells emerged from WT cells but infrequently arose from FANCD2 KO cells (Figures 6D and 6E). FISH confirmed most MTX-resistant WT cells harbored ecDNAs derived from chromosome 5 containing the *DHFR* locus, whereas ecDNAs were rarely detected in MTX-resistant FANCD2 KO cells (Figures 6F–6H and S7I). These cells likely developed resistance to MTX through non-chromothripsis-related mechanisms, including impairments in drug transporters.[58] To determine whether the FA pathway is required for the maintenance of ecDNAs, we examined two cancer cell lines (PC3 and COLO320DM) with established *MYC*-amplified ecDNAs. Loss of FANCD2 (Figure S7J) followed by a month in culture revealed no differences in ecDNA levels (Figures S7K and S7L), demonstrating that FA-induced chromothripsis is a driver of initial ecDNA formation but is dispensable for its propagation and long-term maintenance.

The FA pathway promotes acquired resistance to targeted therapy in melanoma

We next evaluated the contribution of the FA pathway to the genomic evolution of acquired resistance to clinically relevant targeted therapies. Cutaneous melanoma ranks high as a chromothripsis-laden cancer,[2,3] and despite BRAF-targeted cancer therapy being first developed against $BRAF^{V600E}$ melanoma, acquired resistance occurs in the majority of patients. We recently showed that acquired resistance to BRAF-targeted therapy is driven by ecDNAs and complex intra-chromosomal amplicons, including homogeneously staining regions (HSRs), which are dynamic amplicon states often with clonal relationships to tumor-matched chromothriptic events.[22,59,60] To understand how FA-mediated chromothripsis and ecDNA formation contribute to therapy-induced genomic instability and resistance evolution in human malignancies, we targeted *FANCD2* with pairs of sgRNAs in three patient-derived melanoma cell lines harboring $BRAF^{V600E}$ (Figure S8A). FANCD2 inactivation did not alter basal clonogenic growth of $BRAF^{V600E}$ melanoma cells but consistently suppressed the emergence of clones with acquired resistance to chronic BRAF-targeted therapy composed of a mutant BRAF inhibitor (vemurafenib) plus MEK inhibitor (selumetinib) (Figure 6I).

(K) Quantification of metaphases with detectable ecDNA structures as visualized by YOYO-1 staining from (J). Data represent frequency from the indicated number of metaphases pooled from multiple plates as needed; statistical analysis by Fisher's exact test.
See also Figures S7 and S8.

As heterogeneous ecDNAs drive acquired resistance to BRAF-targeted therapy, we tested the hypothesis that disruption of chromothripsis by inactivating FANCD2 would suppress the outgrowth of acquired-resistant cells harboring ecDNAs. As expected, analysis of metaphase spreads stained with YOYO-1 revealed that chronic BRAF-targeted therapy increased the frequency of ecDNA-containing cells (~20%–30%) among the acquired-resistant WT populations compared with vehicle-treated parental lines (<5%; Figures 6J and S8B). The number of ecDNAs detected per metaphase was expectedly heterogeneous, ranging from a few to over 20 per cell (Figures 6J and S8B). Importantly, in agreement with observations from the MTX system, there were sharp reductions in the frequencies of ecDNA-positive metaphases among the rare drug-resistant cells in all three acquired-resistant *BRAF*^{V600E} melanoma populations lacking FANCD2 (Figures 6K and S8C).

As *BRAF* amplification[61] via re-integration of ecDNAs as HSRs[22] drives acquired resistance in two of the three *BRAF*^{V600E} melanoma cell lines, we performed DNA FISH on metaphase spreads using bacterial artificial chromosome (BAC) probes targeting the *BRAF* locus. Consistent with the detection of ecDNAs, similar reductions in therapy-elicited cells harboring *BRAF*-positive HSRs were observed in the absence of FANCD2 (Figures S8D and S8E). Although the FA pathway may protect a subset of early melanoma cells from replication stress-induced death during the first few days of BRAF-targeted therapy,[62] our findings analyzing the karyotypic landscape of long-term "escapee" cells support an additional role of the FA pathway in driving genomic diversification and acquired resistance. Altogether, these data demonstrate that FA-mediated chromothripsis promotes the formation of cancer-associated genomic rearrangements and clinically relevant ecDNAs using a range of experimental models.

DISCUSSION

We conducted unbiased CRISPR-Cas9 screens and uncovered the FA pathway as a requirement for chromothripsis from mitotic errors that generate micronuclei and micronuclei-like nuclear structures. This uncharacterized function of the FA pathway is independent of any observable consequences on micronuclei during interphase. We propose a model in which micronucleated chromosomes enter mitosis in an under-replicated state, which are recognized by the FA pathway as abnormal replication intermediates that require processing via excision and repair of the DNA lesion. Instead, engagement by FANCD2 inadvertently promotes widespread shattering of the micronucleated chromosome through nucleolytic cleavage by the SLX4-XPF-ERCC1 endonuclease. This cascade is activated upon canonical mono-ubiquitination of the FANCI-FANCD2 heterodimer by the FA core complex. Following chromosome shattering, the resulting DNA fragments are subjected to POLD3-dependent MiDAS, which converts tracts of ssDNA into DSB ends that are compatible for ligation by NHEJ (Figure 7). The extent to which MiDAS completes duplication of the initially under-replicated chromosome or whether replication is completed in the ensuing interphase warrants further investigation. Interestingly, it is worth noting that FANCI-FANCD2 does not appear to be involved in TRAIP-dependent mitotic fork breakage in *Xenopus* egg extract systems,[63] highlighting potential differences between experimental systems.

Our work further distinguishes between two unique sources of instability originating within micronuclei during interphase that can trigger chromothripsis: DNA damage and DNA replication defects. In the absence of a functional FA pathway, a fraction of micronucleated chromosomes continue to experience a less extensive form of mitotic chromosome shattering (Figures 1F, 1G, 2E, and 2F). This could arise from micronuclear DSBs acquired during interphase through the action of multiple cytoplasmic nucleases; for example, via the processing of RNA-DNA hybrids by the BER pathway.[15] It will be important to distinguish the contributions between nuclease-mediated interphase DNA damage from replicative defects that provoke mitotic chromosome shattering to chromothriptic rearrangements in cancer genomes. The mechanisms reported here may also explain several genomic features associated with chromothripsis, including the association of rearrangement breakpoints with late-replicating regions of the genome[64] or a hypermutation signature known as kataegis through APOBEC-mediated processing of ssDNA.[2,7,9,52]

Several notable parallels can be drawn between the genome-maintenance function of the FA pathway in protecting late-replicating CFSs from instability[65] and the pathological function of the FA pathway in triggering chromothripsis described in this study (Figure 7). Under conditions of mild replication stress, CFSs are unable to complete timely DNA replication, accumulate FANCD2 foci, and manifest as visible breaks or gaps on mitotic chromosomes.[65] These regions undergo controlled cleavage by GEN1 and/or SLX4-associated nucleases (e.g., MUS81-EME1 and XPF-ERCC1), followed by POLD3-dependent MiDAS, which can prevent the formation of ultrafine anaphase bridges arising from catenated DNA intermediates linking sister chromatids.[35–38,48] This process can also be mutagenic under instances in which under-replicated CFS lesions are repaired by DNA polymerase theta-mediated end joining during mitosis.[63,66] We propose that the mitotic shattering of under-replicated chromosomes from micronuclei is analogous to the intentional breakage of CFS loci, albeit on a chromosome-wide scale, thereby inducing chromothripsis (Figure 7). In this context, the precise structure of the DNA replication intermediate(s) that are processed by XPF-ERCC1—a 3′-flap endonuclease—remains unclear but could include the leading/lagging strand(s) of stalled replication forks and/or potential secondary structures such as RNA-DNA hybrids accumulating in micronuclei.[15] These findings highlight the dichotomous functions of the FA pathway in promoting or suppressing genome stability depending on the context of the lesion that triggers its activation.

Our model predicts that tumors from FA patients harboring germline biallelic FA mutations would lack the signatures of chromothripsis. A comprehensive interrogation of chromothripsis in FA-deficient cancer genomes, however, has been challenging due to the rarity of available tumor specimens derived from FA patients. Among the limited number of samples to date, the majority of patients whose cancers had available whole-genome sequencing data have undergone allogeneic hematopoietic

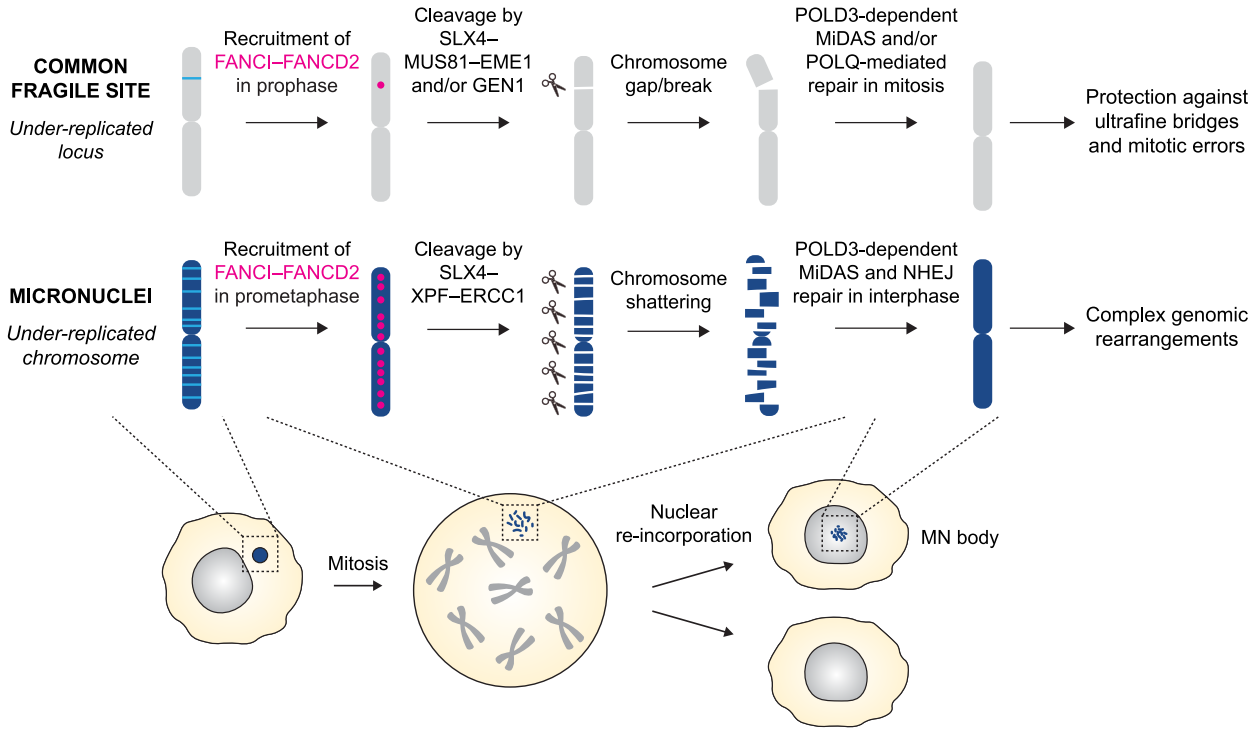

Figure 7. Chromothripsis from mitotic errors is analogous to the controlled processing of under-replicated common fragile sites, albeit on a chromosome-wide scale

Mechanistic parallels between the intentional cleavage of late-replicating CFS loci to promote genome stability (top) and the inadvertent shattering of under-replicated chromosomes from micronuclei to promote genome instability (bottom).

stem cell transplantation,[40] hampering the distinction between cancer-specific alterations from germline polymorphisms from the bone marrow donor. Nonetheless, initial genomic characterization of squamous cell carcinomas from FA patients revealed high numbers of structural variants often organized in chains[40]—a picture distinct from the signatures of canonical or balanced chromothripsis associated with FA-proficient tumors.[67]

This study extends upon a paradoxical connection between chromothripsis and intrinsic mechanisms that have evolved to safeguard mammalian cells against invasion by foreign pathogens[14] or genomic instability.[15] The extent to which these mechanisms contribute to tumorigenesis remain to be determined, as well as whether the FA pathway represents a viable clinical target to prevent chromothripsis, chromosomal abnormalities, and/or ecDNA-mediated drug resistance. Our model suggests that inhibition of the FA pathway may suppress cancer genome evolution in certain chromothripsis-prone cancers in response to therapies and prevent acquired resistance. Lastly, the cohort of genes identified by the screen (Figure 1B; Table S1) provides a unique resource of additional genetic pathways to explore, the majority of which have no reported functions in micronuclei biology or chromothripsis.

Limitations of the study

The cytogenetic methods used in this study offer evidence that micronuclei-mediated complex genomic rearrangements are suppressed in cells lacking a functional FA pathway. However, we cannot formally exclude potential differences in rearrangement patterns that escaped detection by microscopy-based approaches. Whole-genome sequencing of individual clones derived from FA-deficient cells, which harbor mostly simple alterations, may provide higher-resolution views of the genomic rearrangement landscape associated with mitotic errors in the presence or absence of an intact FA pathway.

STAR★METHODS

Detailed methods are provided in the online version of this paper and include the following:

- KEY RESOURCES TABLE
- RESOURCE AVAILABILITY
  - Lead contact
  - Materials availability
  - Data and code availability
- EXPERIMENTAL MODEL AND STUDY PARTICIPANT DETAILS
- METHOD DETAILS
  - Cell culture and reagents
  - CRISPR editing
  - CRISPR-Cas9 screening
  - Immunofluorescence and EdU staining
  - Non-denaturing BrdU
  - Metaphase spread preparation
  - DNA fluorescence in situ hybridization (FISH)
  - Y chromosome shattering and rearrangement assays

SUPPLEMENTAL INFORMATION

Supplemental information can be found online at https://doi.org/10.1016/j.cell.2024.08.001.

ACKNOWLEDGMENTS

We thank Daniel Durocher, Emily Hatch, Gary Kupfer, John Maciejowski, and Sihan Wu for reagents; Anthony Davis and Samuel McBrayer for discussions; Jian Xu and the UT Southwestern Children's Research Institute for assistance with sequencing; and AJ Murphy for technical assistance. We acknowledge the UT Southwestern Quantitative Light Microscopy Core (P30CA142543) and Flow Cytometry Core for shared use of equipment. This work was supported by the US National Institutes of Health (R01CA289435 and R35GM146610 to P.L.; F31CA295091 to J.L.E.; and U54CA274509, P01CA244118, and R01CA176111 to R.S.L.), the Cancer Prevention and Research Institute of Texas (RR180050 to P.L. and RP210041 to J.L.E.), the Welch Foundation (I-2071-20240404 to P.L.), the V Foundation for Cancer Research (T2023-012 to R.S.L.), the Melanoma Research Alliance (924774 to R.S.L.; 1156762 to X.Z.), and a Jonsson Comprehensive Cancer Center Fellowship to Y.W.

AUTHOR CONTRIBUTIONS

J.L.E. and P.L. conceived the project and designed the experiments. J.L.E., X.Z., M.W., Y.W., J.E.V.-I., Q.H., and K.S.W. performed experiments and/or analyzed the data. M.A.S. and A.S. provided critical input. J.L.E. and J.C. analyzed the screen. I.C.-C., R.S.L., and P.L. provided supervision. J.L.E. and P.L. wrote the manuscript with input from all authors.

DECLARATION OF INTERESTS

R.S.L. has received research funding from Day One Biopharmaceuticals, Inc. and clinical trial funding and honorarium from Pfizer, Inc.

Received: November 14, 2023
Revised: May 30, 2024
Accepted: August 5, 2024
Published: August 23, 2024

REFERENCES

1. Stephens, P.J., Greenman, C.D., Fu, B., Yang, F., Bignell, G.R., Mudie, L.J., Pleasance, E.D., Lau, K.W., Beare, D., Stebbings, L.A., et al. (2011). Massive genomic rearrangement acquired in a single catastrophic event during cancer development. Cell *144*, 27–40. https://doi.org/10.1016/j.cell.2010.11.055.
2. Cortés-Ciriano, I., Lee, J.J.K., Xi, R., Jain, D., Jung, Y.L., Yang, L., Gordenin, D., Klimczak, L.J., Zhang, C.Z., Pellman, D.S., et al. (2020). Comprehensive analysis of chromothripsis in 2,658 human cancers using whole-genome sequencing. Nat. Genet. *52*, 331–341. https://doi.org/10.1038/s41588-019-0576-7.
3. Voronina, N., Wong, J.K.L., Hübschmann, D., Hlevnjak, M., Uhrig, S., Heilig, C.E., Horak, P., Kreutzfeldt, S., Mock, A., Stenzinger, A., et al. (2020). The landscape of chromothripsis across adult cancer types. Nat. Commun. *11*, 2320. https://doi.org/10.1038/s41467-020-16134-7.
4. Crasta, K., Ganem, N.J., Dagher, R., Lantermann, A.B., Ivanova, E.V., Pan, Y., Nezi, L., Protopopov, A., Chowdhury, D., and Pellman, D. (2012). DNA breaks and chromosome pulverization from errors in mitosis. Nature *482*, 53–58. https://doi.org/10.1038/nature10802.
5. Zhang, C.Z., Spektor, A., Cornils, H., Francis, J.M., Jackson, E.K., Liu, S., Meyerson, M., and Pellman, D. (2015). Chromothripsis from DNA damage in micronuclei. Nature *522*, 179–184. https://doi.org/10.1038/nature14493.
6. Ly, P., Teitz, L.S., Kim, D.H., Shoshani, O., Skaletsky, H., Fachinetti, D., Page, D.C., and Cleveland, D.W. (2017). Selective Y centromere inactivation triggers chromosome shattering in micronuclei and repair by non-homologous end joining. Nat. Cell Biol. *19*, 68–75. https://doi.org/10.1038/ncb3450.
7. Ly, P., Brunner, S.F., Shoshani, O., Kim, D.H., Lan, W., Pyntikova, T., Flanagan, A.M., Behjati, S., Page, D.C., Campbell, P.J., and Cleveland, D.W. (2019). Chromosome segregation errors generate a diverse spectrum of simple and complex genomic rearrangements. Nat. Genet. *51*, 705–715. https://doi.org/10.1038/s41588-019-0360-8.
8. Mazzagatti, A., Engel, J.L., and Ly, P. (2024). Boveri and beyond: Chromothripsis and genomic instability from mitotic errors. Mol. Cell *84*, 55–69. https://doi.org/10.1016/j.molcel.2023.11.002.
9. Maciejowski, J., Li, Y., Bosco, N., Campbell, P.J., and de Lange, T. (2015). Chromothripsis and Kataegis Induced by Telomere Crisis. Cell *163*, 1641–1654. https://doi.org/10.1016/j.cell.2015.11.054.
10. Umbreit, N.T., Zhang, C.Z., Lynch, L.D., Blaine, L.J., Cheng, A.M., Tourdot, R., Sun, L., Almubarak, H.F., Judge, K., Mitchell, T.J., et al. (2020). Mechanisms generating cancer genome complexity from a single cell division error. Science *368*, eaba0712. https://doi.org/10.1126/science.aba0712.
11. Shoshani, O., Brunner, S.F., Yaeger, R., Ly, P., Nechemia-Arbely, Y., Kim, D.H., Fang, R., Castillon, G.A., Yu, M., Li, J.S.Z., et al. (2021). Chromothripsis drives the evolution of gene amplification in cancer. Nature *591*, 137–141. https://doi.org/10.1038/s41586-020-03064-z.
12. Hatch, E.M., Fischer, A.H., Deerinck, T.J., and Hetzer, M.W. (2013). Catastrophic nuclear envelope collapse in cancer cell micronuclei. Cell *154*, 47–60. https://doi.org/10.1016/j.cell.2013.06.007.
13. Liu, S., Kwon, M., Mannino, M., Yang, N., Renda, F., Khodjakov, A., and Pellman, D. (2018). Nuclear envelope assembly defects link mitotic errors to chromothripsis. Nature *561*, 551–555. https://doi.org/10.1038/s41586-018-0534-z.
14. Mohr, L., Toufektchan, E., von Morgen, P., Chu, K., Kapoor, A., and Maciejowski, J. (2021). ER-directed TREX1 limits cGAS activation at micronuclei. Mol. Cell *81*, 724–738.e9. https://doi.org/10.1016/j.molcel.2020.12.037.
15. Tang, S., Stokasimov, E., Cui, Y., and Pellman, D. (2022). Breakage of cytoplasmic chromosomes by pathological DNA base excision repair. Nature *606*, 930–936. https://doi.org/10.1038/s41586-022-04767-1.
16. Minocherhomji, S., Ying, S., Bjerregaard, V.A., Bursomanno, S., Aleliunaite, A., Wu, W., Mankouri, H.W., Shen, H., Liu, Y., and Hickson, I.D. (2015). Replication stress activates DNA repair synthesis in mitosis. Nature *528*, 286–290. https://doi.org/10.1038/nature16139.
17. Bhowmick, R., Hickson, I.D., and Liu, Y. (2023). Completing genome replication outside of S phase. Mol. Cell *83*, 3596–3607. https://doi.org/10.1016/j.molcel.2023.08.023.
18. Lin, Y.F., Hu, Q., Mazzagatti, A., Valle-Inclán, J.E., Maurais, E.G., Dahiya, R., Guyer, A., Sanders, J.T., Engel, J.L., Nguyen, G., et al. (2023). Mitotic clustering of pulverized chromosomes from micronuclei. Nature *618*, 1041–1048. https://doi.org/10.1038/s41586-023-05974-0.
19. Trivedi, P., Steele, C.D., Au, F.K.C., Alexandrov, L.B., and Cleveland, D.W. (2023). Mitotic tethering enables inheritance of shattered micronuclear chromosomes. Nature *618*, 1049–1056. https://doi.org/10.1038/s41586-023-06216-z.
20. Hu, Q., Espejo Valle-Inclán, J., Dahiya, R., Guyer, A., Mazzagatti, A., Maurais, E.G., Engel, J.L., Lu, H., Davis, A.J., Cortés-Ciriano, I., and Ly, P. (2024). Non-homologous end joining shapes the genomic rearrangement landscape of chromothripsis from mitotic errors. Nat. Commun. *15*, 5611. https://doi.org/10.1038/s41467-024-49985-5.
21. Nathanson, D.A., Gini, B., Mottahedeh, J., Visnyei, K., Koga, T., Gomez, G., Eskin, A., Hwang, K., Wang, J., Masui, K., et al. (2014). Targeted

therapy resistance mediated by dynamic regulation of extrachromosomal mutant EGFR DNA. Science *343*, 72–76. https://doi.org/10.1126/science.1241328.

22. Dharanipragada, P., Zhang, X., Liu, S., Lomeli, S.H., Hong, A., Wang, Y., Yang, Z., Lo, K.Z., Vega-Crespo, A., Ribas, A., et al. (2023). Blocking Genomic Instability Prevents Acquired Resistance to MAPK Inhibitor Therapy in Melanoma. Cancer Discov. *13*, 880–909. https://doi.org/10.1158/2159-8290.CD-22-0787.
23. Pal Choudhuri, S., Girard, L., Lim, J.Y.S., Wise, J.F., Freitas, B., Yang, D., Wong, E., Hamilton, S., Chien, V.D., Kim, Y.J., et al. (2024). Acquired Cross-Resistance in Small Cell Lung Cancer due to Extrachromosomal DNA Amplification of MYC Paralogs. Cancer Discov. *14*, 804–827. https://doi.org/10.1158/2159-8290.CD-23-0656.
24. Knipscheer, P., Räschle, M., Smogorzewska, A., Enoiu, M., Ho, T.V., Schärer, O.D., Elledge, S.J., and Walter, J.C. (2009). The Fanconi anemia pathway promotes replication-dependent DNA interstrand cross-link repair. Science *326*, 1698–1701. https://doi.org/10.1126/science.1182372.
25. Garcia-Higuera, I., Taniguchi, T., Ganesan, S., Meyn, M.S., Timmers, C., Hejna, J., Grompe, M., and D'Andrea, A.D. (2001). Interaction of the Fanconi anemia proteins and BRCA1 in a common pathway. Mol. Cell *7*, 249–262. https://doi.org/10.1016/s1097-2765(01)00173-3.
26. Smogorzewska, A., Matsuoka, S., Vinciguerra, P., McDonald, E.R., 3rd, Hurov, K.E., Luo, J., Ballif, B.A., Gygi, S.P., Hofmann, K., D'Andrea, A.D., and Elledge, S.J. (2007). Identification of the FANCI protein, a monoubiquitinated FANCD2 paralog required for DNA repair. Cell *129*, 289–301. https://doi.org/10.1016/j.cell.2007.03.009.
27. Wang, R., Wang, S., Dhar, A., Peralta, C., and Pavletich, N.P. (2020). DNA clamp function of the monoubiquitinated Fanconi anaemia ID complex. Nature *580*, 278–282. https://doi.org/10.1038/s41586-020-2110-6.
28. Alcón, P., Shakeel, S., Chen, Z.A., Rappsilber, J., Patel, K.J., and Passmore, L.A. (2020). FANCD2-FANCI is a clamp stabilized on DNA by monoubiquitination of FANCD2 during DNA repair. Nat. Struct. Mol. Biol. *27*, 240–248. https://doi.org/10.1038/s41594-020-0380-1.
29. Kim, Y., Lach, F.P., Desetty, R., Hanenberg, H., Auerbach, A.D., and Smogorzewska, A. (2011). Mutations of the SLX4 gene in Fanconi anemia. Nat. Genet. *43*, 142–146. https://doi.org/10.1038/ng.750.
30. Klein Douwel, D., Boonen, R.A.C.M., Long, D.T., Szypowska, A.A., Räschle, M., Walter, J.C., and Knipscheer, P. (2014). XPF-ERCC1 acts in Unhooking DNA interstrand crosslinks in cooperation with FANCD2 and FANCP/SLX4. Mol. Cell *54*, 460–471. https://doi.org/10.1016/j.molcel.2014.03.015.
31. Schlacher, K., Wu, H., and Jasin, M. (2012). A distinct replication fork protection pathway connects Fanconi anemia tumor suppressors to RAD51-BRCA1/2. Cancer Cell *22*, 106–116. https://doi.org/10.1016/j.ccr.2012.05.015.
32. Madireddy, A., Kosiyatrakul, S.T., Boisvert, R.A., Herrera-Moyano, E., García-Rubio, M.L., Gerhardt, J., Vuono, E.A., Owen, N., Yan, Z., Olson, S., et al. (2016). FANCD2 Facilitates Replication through Common Fragile Sites. Mol. Cell *64*, 388–404. https://doi.org/10.1016/j.molcel.2016.09.017.
33. Chang, E.Y.C., Tsai, S., Aristizabal, M.J., Wells, J.P., Coulombe, Y., Busatto, F.F., Chan, Y.A., Kumar, A., Dan Zhu, Y., Wang, A.Y.H., et al. (2019). MRE11-RAD50-NBS1 promotes Fanconi Anemia R-loop suppression at transcription-replication conflicts. Nat. Commun. *10*, 4265. https://doi.org/10.1038/s41467-019-12271-w.
34. Elango, R., Panday, A., Lach, F.P., Willis, N.A., Nicholson, K., Duffey, E.E., Smogorzewska, A., and Scully, R. (2022). The structure-specific endonuclease complex SLX4-XPF regulates Tus-Ter-induced homologous recombination. Nat. Struct. Mol. Biol. *29*, 801–812. https://doi.org/10.1038/s41594-022-00812-9.
35. Chan, K.L., Palmai-Pallag, T., Ying, S., and Hickson, I.D. (2009). Replication stress induces sister-chromatid bridging at fragile site loci in mitosis. Nat. Cell Biol. *11*, 753–760. https://doi.org/10.1038/ncb1882.
36. Naim, V., and Rosselli, F. (2009). The FANC pathway and BLM collaborate during mitosis to prevent micro-nucleation and chromosome abnormalities. Nat. Cell Biol. *11*, 761–768. https://doi.org/10.1038/ncb1883.
37. Ying, S., Minocherhomji, S., Chan, K.L., Palmai-Pallag, T., Chu, W.K., Wass, T., Mankouri, H.W., Liu, Y., and Hickson, I.D. (2013). MUS81 promotes common fragile site expression. Nat. Cell Biol. *15*, 1001–1007. https://doi.org/10.1038/ncb2773.
38. Naim, V., Wilhelm, T., Debatisse, M., and Rosselli, F. (2013). ERCC1 and MUS81-EME1 promote sister chromatid separation by processing late replication intermediates at common fragile sites during mitosis. Nat. Cell Biol. *15*, 1008–1015. https://doi.org/10.1038/ncb2793.
39. Alter, B.P., Giri, N., Savage, S.A., and Rosenberg, P.S. (2018). Cancer in the National Cancer Institute inherited bone marrow failure syndrome cohort after fifteen years of follow-up. Haematologica *103*, 30–39. https://doi.org/10.3324/haematol.2017.178111.
40. Webster, A.L.H., Sanders, M.A., Patel, K., Dietrich, R., Noonan, R.J., Lach, F.P., White, R.R., Goldfarb, A., Hadi, K., Edwards, M.M., et al. (2022). Genomic signature of Fanconi anaemia DNA repair pathway deficiency in cancer. Nature *612*, 495–502. https://doi.org/10.1038/s41586-022-05253-4.
41. Sasaki, M.S., and Tonomura, A. (1973). A high susceptibility of Fanconi's anemia to chromosome breakage by DNA cross-linking agents. Cancer Res. *33*, 1829–1836.
42. Su, D., Feng, X., Colic, M., Wang, Y., Zhang, C., Wang, C., Tang, M., Hart, T., and Chen, J. (2020). CRISPR/CAS9-based DNA damage response screens reveal gene-drug interactions. DNA Repair (Amst) *87*, 102803. https://doi.org/10.1016/j.dnarep.2020.102803.
43. Kim, Y., Spitz, G.S., Veturi, U., Lach, F.P., Auerbach, A.D., and Smogorzewska, A. (2013). Regulation of multiple DNA repair pathways by the Fanconi anemia protein SLX4. Blood *121*, 54–63. https://doi.org/10.1182/blood-2012-07-441212.
44. Wyatt, H.D.M., Sarbajna, S., Matos, J., and West, S.C. (2013). Coordinated actions of SLX1-SLX4 and MUS81-EME1 for Holliday junction resolution in human cells. Mol. Cell *52*, 234–247. https://doi.org/10.1016/j.molcel.2013.08.035.
45. Wyatt, H.D.M., Laister, R.C., Martin, S.R., Arrowsmith, C.H., and West, S.C. (2017). The SMX DNA Repair Tri-nuclease. Mol. Cell *65*, 848–860.e11. https://doi.org/10.1016/j.molcel.2017.01.031.
46. Regairaz, M., Zhang, Y.W., Fu, H., Agama, K.K., Tata, N., Agrawal, S., Aladjem, M.I., and Pommier, Y. (2011). Mus81-mediated DNA cleavage resolves replication forks stalled by topoisomerase I-DNA complexes. J. Cell Biol. *195*, 739–749. https://doi.org/10.1083/jcb.201104003.
47. Chan, Y.W., and West, S.C. (2014). Spatial control of the GEN1 Holliday junction resolvase ensures genome stability. Nat. Commun. *5*, 4844. https://doi.org/10.1038/ncomms5844.
48. Benitez, A., Sebald, M., Kanagaraj, R., Rodrigo-Brenni, M.C., Chan, Y.W., Liang, C.C., and West, S.C. (2023). GEN1 promotes common fragile site expression. Cell Rep. *42*, 112062. https://doi.org/10.1016/j.celrep.2023.112062.
49. van Wietmarschen, N., Sridharan, S., Nathan, W.J., Tubbs, A., Chan, E.M., Callen, E., Wu, W., Belinky, F., Tripathi, V., Wong, N., et al. (2020). Repeat expansions confer WRN dependence in microsatellite-unstable cancers. Nature *586*, 292–298. https://doi.org/10.1038/s41586-020-2769-8.
50. Glover, T.W., Berger, C., Coyle, J., and Echo, B. (1984). DNA polymerase alpha inhibition by aphidicolin induces gaps and breaks at common fragile sites in human chromosomes. Hum. Genet. *67*, 136–142. https://doi.org/10.1007/BF00272988.
51. Duda, H., Arter, M., Gloggnitzer, J., Teloni, F., Wild, P., Blanco, M.G., Altmeyer, M., and Matos, J. (2016). A Mechanism for Controlled Breakage of Under-replicated Chromosomes during Mitosis. Dev. Cell *39*, 740–755. https://doi.org/10.1016/j.devcel.2016.11.017.
52. Maciejowski, J., Chatzipli, A., Dananberg, A., Chu, K., Toufektchan, E., Klimczak, L.J., Gordenin, D.A., Campbell, P.J., and de Lange, T. (2020).

APOBEC3-dependent kataegis and TREX1-driven chromothripsis during telomere crisis. Nat. Genet. *52*, 884–890. https://doi.org/10.1038/s41588-020-0667-5.

53. Papathanasiou, S., Mynhier, N.A., Liu, S., Brunette, G., Stokasimov, E., Jacob, E., Li, L., Comenho, C., van Steensel, B., Buenrostro, J.D., et al. (2023). Heritable transcriptional defects from aberrations of nuclear architecture. Nature *619*, 184–192. https://doi.org/10.1038/s41586-023-06157-7.

54. Kim, H., Nguyen, N.P., Turner, K., Wu, S., Gujar, A.D., Luebeck, J., Liu, J., Deshpande, V., Rajkumar, U., Namburi, S., et al. (2020). Extrachromosomal DNA is associated with oncogene amplification and poor outcome across multiple cancers. Nat. Genet. *52*, 891–897. https://doi.org/10.1038/s41588-020-0678-2.

55. Rosswog, C., Bartenhagen, C., Welte, A., Kahlert, Y., Hemstedt, N., Lorenz, W., Cartolano, M., Ackermann, S., Perner, S., Vogel, W., et al. (2021). Chromothripsis followed by circular recombination drives oncogene amplification in human cancer. Nat. Genet. *53*, 1673–1685. https://doi.org/10.1038/s41588-021-00951-7.

56. Alt, F.W., Kellems, R.E., Bertino, J.R., and Schimke, R.T. (1978). Selective multiplication of dihydrofolate reductase genes in methotrexate-resistant variants of cultured murine cells. J. Biol. Chem. *253*, 1357–1370.

57. Kaufman, R.J., Brown, P.C., and Schimke, R.T. (1979). Amplified dihydrofolate reductase genes in unstably methotrexate-resistant cells are associated with double minute chromosomes. Proc. Natl. Acad. Sci. USA *76*, 5669–5673. https://doi.org/10.1073/pnas.76.11.5669.

58. Bertino, J.R., Göker, E., Gorlick, R., Li, W.W., and Banerjee, D. (1996). Resistance mechanisms to methotrexate in tumors. Stem Cells *14*, 5–9.

59. Song, K., Minami, J.K., Huang, A., Dehkordi, S.R., Lomeli, S.H., Luebeck, J., Goodman, M.H., Moriceau, G., Krijgsman, O., Dharanipragada, P., et al. (2022). Plasticity of Extrachromosomal and Intrachromosomal BRAF Amplifications in Overcoming Targeted Therapy Dosage Challenges. Cancer Discov. *12*, 1046–1069. https://doi.org/10.1158/2159-8290.CD-20-0936.

60. Liu, S., Dharanipragada, P., Lomeli, S.H., Wang, Y., Zhang, X., Yang, Z., Lim, R.J., Dumitras, C., Scumpia, P.O., Dubinett, S.M., et al. (2023). Multi-organ landscape of therapy-resistant melanoma. Nat. Med. *29*, 1123–1134. https://doi.org/10.1038/s41591-023-02304-9.

61. Shi, H., Moriceau, G., Kong, X., Lee, M.K., Lee, H., Koya, R.C., Ng, C., Chodon, T., Scolyer, R.A., Dahlman, K.B., et al. (2012). Melanoma whole-exome sequencing identifies (V600E)B-RAF amplification-mediated acquired B-RAF inhibitor resistance. Nat. Commun. *3*, 724. https://doi.org/10.1038/ncomms1727.

62. Hoffman, T.E., Nangia, V., III, C.R., Passanisi, V.J., Armstrong, C., Yang, C., and Spencer, S.L. (2023). Multiple cancers escape from multiple MAPK pathway inhibitors and use DNA replication stress signaling to tolerate aberrant cell cycles. Sci. Signal. *16*, eade8744. https://doi.org/10.1126/scisignal.ade8744.

63. Deng, L., Wu, R.A., Sonneville, R., Kochenova, O.V., Labib, K., Pellman, D., and Walter, J.C. (2019). Mitotic CDK Promotes Replisome Disassembly, Fork Breakage, and Complex DNA Rearrangements. Mol. Cell *73*, 915–929.e6. https://doi.org/10.1016/j.molcel.2018.12.021.

64. Chatron, N., Giannuzzi, G., Rollat-Farnier, P.-A., Diguet, F., Porcu, E., Yammine, T., Uguen, K., Bellil, Z.-L., Zillhardt, J.L., Sorlin, A., et al. (2020). The enrichment of breakpoints in late-replicating chromatin provides novel insights into chromoanagenesis mechanisms. Preprint at bioRxiv. https://doi.org/10.1101/2020.07.17.206771.

65. Howlett, N.G., Taniguchi, T., Durkin, S.G., D'Andrea, A.D., and Glover, T.W. (2005). The Fanconi anemia pathway is required for the DNA replication stress response and for the regulation of common fragile site stability. Hum. Mol. Genet. *14*, 693–701. https://doi.org/10.1093/hmg/ddi065.

66. Wilson, T.E., Ahmed, S., Winningham, A., and Glover, T.W. (2024). POLQ mediates replication-stress induced structural variant formation throughout common fragile sites during mitosis. Preprint at bioRxiv. https://doi.org/10.1101/2024.05.28.596214.

67. Korbel, J.O., and Campbell, P.J. (2013). Criteria for inference of chromothripsis in cancer genomes. Cell *152*, 1226–1236. https://doi.org/10.1016/j.cell.2013.02.023.

68. Burns, J.C., Friedmann, T., Driever, W., Burrascano, M., and Yee, J.K. (1993). Vesicular stomatitis virus G glycoprotein pseudotyped retroviral vectors: concentration to very high titer and efficient gene transfer into mammalian and nonmammalian cells. Proc. Natl. Acad. Sci. USA *90*, 8033–8037. https://doi.org/10.1073/pnas.90.17.8033.

69. Álvarez-Quilón, A., Wojtaszek, J.L., Mathieu, M.C., Patel, T., Appel, C.D., Hustedt, N., Rossi, S.E., Wallace, B.D., Setiaputra, D., Adam, S., et al. (2020). Endogenous DNA 3' Blocks Are Vulnerabilities for BRCA1 and BRCA2 Deficiency and Are Reversed by the APE2 Nuclease. Mol. Cell *78*, 1152–1165.e8. https://doi.org/10.1016/j.molcel.2020.05.021.

70. Sanjana, N.E., Shalem, O., and Zhang, F. (2014). Improved vectors and genome-wide libraries for CRISPR screening. Nat. Methods *11*, 783–784. https://doi.org/10.1038/nmeth.3047.

71. Ran, F.A., Hsu, P.D., Wright, J., Agarwala, V., Scott, D.A., and Zhang, F. (2013). Genome engineering using the CRISPR-Cas9 system. Nat. Protoc. *8*, 2281–2308. https://doi.org/10.1038/nprot.2013.143.

72. Gstalder, C., Liu, D., Miao, D., Lutterbach, B., DeVine, A.L., Lin, C., Shettigar, M., Pancholi, P., Buchbinder, E.I., Carter, S.L., et al. (2020). Inactivation of Fbxw7 Impairs dsRNA Sensing and Confers Resistance to PD-1 Blockade. Cancer Discov. *10*, 1296–1311. https://doi.org/10.1158/2159-8290.CD-19-1416.

73. Stewart, S.A., Dykxhoorn, D.M., Palliser, D., Mizuno, H., Yu, E.Y., An, D.S., Sabatini, D.M., Chen, I.S.Y., Hahn, W.C., Sharp, P.A., et al. (2003). Lentivirus-delivered stable gene silencing by RNAi in primary cells. RNA *9*, 493–501. https://doi.org/10.1261/rna.2192803.

74. Schindelin, J., Arganda-Carreras, I., Frise, E., Kaynig, V., Longair, M., Pietzsch, T., Preibisch, S., Rueden, C., Saalfeld, S., Schmid, B., et al. (2012). Fiji: an open-source platform for biological-image analysis. Nat. Methods *9*, 676–682. https://doi.org/10.1038/nmeth.2019.

75. Zhou, Y., Zhou, B., Pache, L., Chang, M., Khodabakhshi, A.H., Tanaseichuk, O., Benner, C., and Chanda, S.K. (2019). Metascape provides a biologist-oriented resource for the analysis of systems-level datasets. Nat. Commun. *10*, 1523. https://doi.org/10.1038/s41467-019-09234-6.

76. Horlbeck, M.A., Gilbert, L.A., Villalta, J.E., Adamson, B., Pak, R.A., Chen, Y., Fields, A.P., Park, C.Y., Corn, J.E., Kampmann, M., and Weissman, J.S. (2016). Compact and highly active next-generation libraries for CRISPR-mediated gene repression and activation. eLife *5*, e19760. https://doi.org/10.7554/eLife.19760.

77. Chen, J., Brunner, A.D., Cogan, J.Z., Nuñez, J.K., Fields, A.P., Adamson, B., Itzhak, D.N., Li, J.Y., Mann, M., Leonetti, M.D., and Weissman, J.S. (2020). Pervasive functional translation of noncanonical human open reading frames. Science *367*, 1140–1146. https://doi.org/10.1126/science.aay0262.

78. Lin, Y.F., Hu, Q., Guyer, A., Fachinetti, D., and Ly, P. (2024). Induction of chromosome-specific micronuclei and chromothripsis by centromere inactivation. Methods Cell Biol. *182*, 1–20. https://doi.org/10.1016/bs.mcb.2022.10.009.

STAR★METHODS

KEY RESOURCES TABLE

REAGENT or RESOURCE	SOURCE	IDENTIFIER
Antibodies		
Rabbit polyclonal anti-FANCD2 antibody	Novus Biologicals	Cat# NB100-182
Mouse monoclonal anti-FANCD2 (FI17) antibody	Santa Cruz Biotechnology	Cat# sc-20022
Rabbit polyclonal anti-phospho-histone H2A.X (Ser139) antibody	Cell Signaling Technology	Cat# 2577
Mouse monoclonal anti-phospho-histone H2A.X (Ser139), clone JBW301 antibody	Sigma-Aldrich	Cat# 05-636
Rat monoclonal anti-RPA32/RPA2 (4E4) antibody	Cell Signaling Technology	Cat# 2208
Rabbit polyclonal anti-53BP1 antibody	Novus Biologicals	Cat# NB100-304
Mouse monoclonal anti-RB (4H1) antibody	Cell Signaling Technology	Cat# 9309
Mouse monoclonal anti-BrdU (B44) antibody	BD Biosciences	Cat# 347580
Rabbit polyclonal anti-XPF/ERCC4 antibody	Bethyl	Cat# A301-315A
Rabbit polyclonal anti-LMNB1 antibody	Proteintech	Cat# 12987-1-AP
Mouse monoclonal anti-POLD3 antibody	Abnova	Cat# H00010714-M01
Rabbit monoclonal anti-TREX1 (D8E2O) antibody	Cell Signaling Technology	Cat# 15107
Rabbit polyclonal anti-MPG antibody	Novus Biologicals	Cat# NBP1-82787
Rabbit monoclonal anti-β-actin (13E5) antibody	Cell Signaling Technology	Cat# 4970
Rabbit polyclonal anti-α-tubulin antibody	Cell Signaling Technology	Cat# 2144S
Donkey anti-Mouse IgG (H+L) Highly Cross-Adsorbed Secondary Antibody, Alexa Fluor 488	Invitrogen	Cat# A-21202
Donkey anti-Mouse IgG (H+L) Highly Cross-Adsorbed Secondary Antibody, Alexa Fluor 555	Invitrogen	Cat# A-31570
Donkey anti-Mouse IgG (H+L) Highly Cross-Adsorbed Secondary Antibody, Alexa Fluor 647	Invitrogen	Cat# A-31571
Donkey anti-Rabbit IgG (H+L) Highly Cross-Adsorbed Secondary Antibody, Alexa Fluor 488	Invitrogen	Cat# A-21206
Donkey anti-Rabbit IgG (H+L) Highly Cross-Adsorbed Secondary Antibody, Alexa Fluor™ 555	Invitrogen	Cat# A-31572
Donkey anti-Rabbit IgG (H+L) Highly Cross-Adsorbed Secondary Antibody, Alexa Fluor™ 647	Invitrogen	Cat# A-31573
Donkey anti-Rat IgG (H+L) Highly Cross-Adsorbed Secondary Antibody, Alexa Fluor™ 488	Invitrogen	Cat# A-21208
Bacterial and virus strains		
ElectroMAX STBL4 competent cells	Invitrogen	Cat# 11635018
NEB 5-alpha competent cells	New England Biolabs	Cat# C2987U
Chemicals, peptides, and recombinant proteins		
High-glucose DMEM	Gibco	Cat# 11965092
DMEM/F-12	Gibco	Cat# 11320033
Tetracycline-free fetal bovine serum (FBS)	Omega Scientific	Cat# FB-16
Heat-inactivated fetal bovine serum (FBS)	Gibco	Cat# A5256701

(*Continued on next page*)

Continued

REAGENT or RESOURCE	SOURCE	IDENTIFIER
L-Glutamine	Gibco	Cat# 25030081
Penicillin–streptomycin	Sigma-Aldrich	Cat# P4333
Polybrene	Sigma-Aldrich	Cat# TR-1003
Puromycin	Sigma-Aldrich	Cat# P8833
Doxycycline	Sigma-Aldrich	Cat# D3447
Indole-3-acetic acid sodium salt (auxin)	Sigma-Aldrich	Cat# I5148
Genticin	Gibco	Cat# 15-750-060
Zeocin	InvivoGen	Cat# Ant-zn-05
Nocodazole	Millipore-Sigma	Cat# 487928
Colcemid (KaryoMAX)	Gibco	Cat# 15212012
Reversine (Mps1 inhibitor)	Cayman Chemical	Cat# 10004412
NMS-P715 (Mps1 inhibitor)	Cayman Chemical	Cat# 31613
Mitomycin C	Sigma-Aldrich	Cat# M4287
Methotrexate	Calbiochem	Cat# 454126
Aphidicolin	Cayman Chemical	Cat# 14007
AZD-1775 (WEE1 inhibitor)	MedChemExpress	Cat# HY-10993
Vemurafenib (PLX4032, BRAF inhibitor)	LC Laboratories	Cat# V-2800
Selumetinib (AZD6244, MEK inhibitor)	Selleck Chemicals	Cat# S1008
SuperSignal West Pico Plus	Thermo Scientific	Cat# 34580
5-Bromo-2'-deoxyuridine (BrdU)	Sigma-Aldrich	Cat# B5002
ProLong Gold Antifade Mountant	Invitrogen	Cat# P36930
ProLong Diamond Antifade Mountant with DAPI	Invitrogen	Cat# P36962
YOYO-1	Invitrogen	Cat# Y3601
Critical commercial assays		
Click-iT EdU Cell Proliferation Kit for Imaging, Alexa Fluor 647 dye	Invitrogen	Cat# C10340
Quick-DNA Midiprep Plus Kit	Zymo Research	Cat# D4075
NucleoBond Xtra BAC Kit	Macherey-Nagel	Cat# 740436.25
Nick Translation DNA Labeling System 2.0	Enzo Life Sciences	Cat# ENZ-GEN111-0050
GenePrint 10 System	Promega	Cat# B9510
Experimental models: Cell lines		
DLD-1 CEN-SELECT	Ly et al.[7]	N/A
DLD-1 CEN-SELECT puromycin resistance KO	This study	N/A
DLD-1 CEN-SELECT – LCv2 sgNTC #1 Pool	This study	N/A
DLD-1 CEN-SELECT – LCv2 sgFAAP20 #1 Pool	This study	N/A
DLD-1 CEN-SELECT – LCv2 sgFAAP20 #2 Pool	This study	N/A
DLD-1 CEN-SELECT – LCv2 sgFANCD2 #1 Pool	This study	N/A
DLD-1 CEN-SELECT – LCv2 sgFANCD2 #2 Pool	This study	N/A
DLD-1 CEN-SELECT – LCv2 sgFANCD2 #1 Clone 1	This study	N/A
DLD-1 CEN-SELECT – LCv2 sgFANCD2 #1 Clone 4	This study	N/A
DLD-1 CEN-SELECT – LCv2 sgFANCD2 #1 Clone 1 + pMMP-FANCD2 WT cDNA	This study	N/A
DLD-1 CEN-SELECT – LCv2 sgFANCD2 #1 Clone 1 + pMMP-FANCD2 K561R cDNA	This study	N/A
DLD-1 CEN-SELECT – LCv2 sgXPF #1 Pool	This study	N/A
DLD-1 CEN-SELECT – LCv2 sgXPF #2 Pool	This study	N/A
DLD-1 CEN-SELECT – LCv2 sgFANCM Pool	This study	N/A
DLD-1 CEN-SELECT – LCv2 sgFANCL Pool	This study	N/A

(*Continued on next page*)

Continued

REAGENT or RESOURCE	SOURCE	IDENTIFIER
DLD-1 CEN-SELECT – LCv2 sgFANCA Pool	This study	N/A
DLD-1 CEN-SELECT – LCv2 sgFANCI Pool	This study	N/A
DLD-1 CEN-SELECT – PX459 sgSXL4 #1 Clone 5	This study	N/A
DLD-1 CEN-SELECT – PX459 sgSXL4 #1 Clone 9	This study	N/A
DLD-1 CEN-SELECT – PX459 sgSXL4 #1 Clone 5 + pBABE-SLX4 WT cDNA	This study	N/A
DLD-1 CEN-SELECT – PX459 sgSXL4 #1 Clone 5 + pBABE-SLX4 L530A/W531A cDNA	This study	N/A
DLD-1 CEN-SELECT – LCv2 sgFANCD2 #1 + LG sgFANCD2 #3	This study	N/A
DLD-1 CEN-SELECT – LCv2 sgFANCD2 #2 + LG sgFANCD2 #4	This study	N/A
DLD-1 CEN-SELECT – LCv2 sgXPF #1 + LG sgXPF #3	This study	N/A
DLD-1 CEN-SELECT – LCv2 sgXPF #2 + LG sgXPF #4	This study	N/A
RPE-1 T2p1	John Maciejowski	Maciejowski et al.[9]
RPE-1 T2p1 – PX459 sgNTC #1 Pool	This study	N/A
RPE-1 T2p1 – PX459 sgFANCD2 #1 Clone 2	This study	N/A
RPE-1 hTERT	ATCC	CRL-4000
RPE-1 hTERT – LCv2 sgFANCD2 #1 Pool	This study	N/A
RPE-1 hTERT – LCv2 sgFANCD2 #2 Pool	This study	N/A
HeLa S3	ATCC	CCL-2.2
HeLa S3 – LCV2 sgNTC #1 Pool	This study	N/A
HeLa S3 – LCV2 sgFANCD2 #1 Pool	This study	N/A
HeLa S3 – LCV2 sgFANCD2 #2 Pool	This study	N/A
M229	UCLA	N/A
M249	UCLA	N/A
M395	UCLA	N/A
M229 – LCv2 sgNTC #1 + LG sgNTC #2 Pool	This study	N/A
M229 – LCv2 sgFANCD2 #1 + LG sgFANCD2 #3 Pool	This study	N/A
M229 – LCv2 sgFANCD2 #2 + LG sgFANCD2 #4 Pool	This study	N/A
M249 – LCv2 sgNTC #1 + LG sgNTC #2 Pool	This study	N/A
M249 – LCv2 sgFANCD2 #1 + LG sgFANCD2 #3 Pool	This study	N/A
M249 – LCv2 sgFANCD2 #2 + LG sgFANCD2 #4 Pool	This study	N/A
M395 – LCv2 sgNTC #1 + LG sgNTC #2 Pool	This study	N/A
M395 – LCv2 sgFANCD2 #1 + LG sgFANCD2 #3 Pool	This study	N/A
M395 – LCv2 sgFANCD2 #2 + LG sgFANCD2 #4 Pool	This study	N/A
293T	ATCC	CRL-3216
293GP	Burns et al.[68]	N/A
PC3	Sihan Wu	N/A
COLO320DM	Sihan Wu	N/A
Oligonucleotides		
SLX4 gDNA Forward primer: GGACTCTTGAAACTTGCGTCT	Álvarez-Quilón et al.[69]	N/A
SLX4 gDNA Reverse primer: CGGTACCTTATCAAGGAAGCTA	Álvarez-Quilón et al.[69]	N/A
siRNA targeting sequences: See Table S2	N/A	N/A
CRISPR-Cas9 screen NGS primers: See Table S2	N/A	N/A

(*Continued on next page*)

Continued

REAGENT or RESOURCE	SOURCE	IDENTIFIER
CRISPR-Cas9 sgRNA sequences: See Table S2	N/A	N/A
Recombinant DNA		
pBABE-RFP-NLS	Ly et al.[6]	N/A
pBABE-GFP-SLX4 WT cDNA	Daniel Durocher	Álvarez-Quilón et al.[69]
pBABE-GFP-SLX4 L530A/W531A cDNA	Daniel Durocher	Álvarez-Quilón et al.[69]
pMMP-FLAG-FANCD2 WT cDNA	Gary Kupfer	Garcia-Higuera et al.[25]
pMMP-FLAG-FANCD2 K561R cDNA	Gary Kupfer	Garcia-Higuera et al.[25]
pQCXIB-mCherry	Emily Hatch	Hatch et al.[12]
pQCXIB-mCherry-LMNB2	Emily Hatch	Hatch et al.[12]
pBABE-mCherry-H2B	Lin et al.[18]	N/A
LentiCRISPRv2-puro	Sanjana et al.[70]	Addgene #52961
pX459	Ran et al.[71]	Addgene #62988
LentiGuide-zeo	Gstalder et al.[72]	Addgene #160091
pX458	Ran et al.[71]	Addgene #48138
LentiCRISPRv2-puro – sgNTC #1	This study	N/A
LentiCRISPRv2-puro – sgFAAP20 #1	This study	N/A
LentiCRISPRv2-puro – sgFAAP20 #2	This study	N/A
LentiCRISPRv2-puro – sgFANCD2 #1	This study	N/A
LentiCRISPRv2-puro – sgFANCD2 #2	This study	N/A
LentiCRISPRv2-puro – sgXPF (ERCC4) #1	This study	N/A
LentiCRISPRv2-puro – sgXPF (ERCC4) #1	This study	N/A
LentiCRISPRv2-puro – sgELOA #1	This study	N/A
LentiCRISPRv2-puro – sgELOA #2	This study	N/A
LentiCRISPRv2-puro – sgCHD2 #1	This study	N/A
LentiCRISPRv2-puro – sgCHD2 #2	This study	N/A
LentiCRISPRv2-puro – sgFBXW7 #1	This study	N/A
LentiCRISPRv2-puro – sgFBXW7 #2	This study	N/A
LentiCRISPRv2-puro – sgPOLE4 #1	This study	N/A
LentiCRISPRv2-puro – sgPOLE4 #2	This study	N/A
LentiCRISPRv2-puro – sgPOLE3 #1	This study	N/A
LentiCRISPRv2-puro – sgPOLE3 #2	This study	N/A
LentiCRISPRv2-puro – sgPIN1 #1	This study	N/A
LentiCRISPRv2-puro – sgPIN1 #2	This study	N/A
LentiCRISPRv2-puro – sgRPA1 #1	This study	N/A
LentiCRISPRv2-puro – sgRPA1 #2	This study	N/A
LentiCRISPRv2-puro – sgFANCM	This study	N/A
LentiCRISPRv2-puro – sgFANCA	This study	N/A
LentiCRISPRv2-puro – sgFANCL	This study	N/A
LentiCRISPRv2-puro – sgFANCI	This study	N/A
LentiCRISPRv2-puro – sgMPG #1	This study	N/A
LentiCRISPRv2-puro – sgMPG #2	This study	N/A
LentiCRISPRv2-puro – sgTREX1 #1	This study	N/A
LentiCRISPRv2-puro – sgTREX1 #2	This study	N/A
pX459 – sgNTC #1	This study	N/A
pX459 – sgFANCD2 #1	This study	N/A
pX459 – sgSLX4 #1	This study	N/A
LentiGuide-zeo – sgNTC #2	This study	N/A
LentiGuide-zeo – sgFANCD2 #3	This study	N/A

(*Continued on next page*)

Continued

REAGENT or RESOURCE	SOURCE	IDENTIFIER
LentiGuide-zeo – sgFANCD2 #4	This study	N/A
LentiGuide-zeo – sgXPF (ERCC4) #3	This study	N/A
LentiGuide-zeo – sgXPF (ERCC4) #4	This study	N/A
pVSV-G	Stewart et al.[73]	Addgene #8454
psPAX2	Didier Trono	Addgene #12260
pMD2.G	Didier Trono	Addgene #12259
DNA Damage Response MKOv4 Library	Su et al.[42]	Addgene #140219
Software and algorithms		
Fiji	Schindelin et al.[74]	N/A
GraphPad Prism v9.5.0	GraphPad Software Inc.	N/A
Adobe Creative Cloud	Adobe Inc.	N/A
Metafer	MetaSystems	N/A
Isis	MetaSystems	N/A
softWorX v.7.2.1	Cytiva	N/A
Metascape	Zhou et al.[75]	N/A
ScreenProcessing	Horlbeck et al.[76]	N/A
Other		
XCP Y Orange DNA FISH probe	MetaSystems	Cat# D-0324-050-OR
XCE X/YqH DNA FISH probe	MetaSystems	Cat# D-0832-050-OG
XCP 5 Orange DNA FISH probe	MetaSystems	Cat# D-0305-050-OR
DHFR locus-specific DNA FISH probe	BACPAC Resources	Cat# RP11-90A9
BRAF locus-specific DNA FISH probe	Empire Genomics	Cat# BRAF-20
Chromosome 7 (CEN7) DNA FISH probe	Empire Genomics	Cat# CHR07-10

RESOURCE AVAILABILITY

Lead contact

Further information and requests for resources and reagents should be directed to and will be fulfilled by the lead contact, Peter Ly (peter.ly@utsouthwestern.edu).

Materials availability

Plasmids and cell lines generated in this study are available upon request.

Data and code availability

- All data reported in this paper will be shared by the lead contact upon request.
- This paper does not report original code.
- Any additional information required to reanalyze the data reported in this paper is available from the lead contact upon request.

EXPERIMENTAL MODEL AND STUDY PARTICIPANT DETAILS

All cell lines were maintained at 37°C under 5% CO_2 and atmospheric oxygen. DLD-1 (male), HeLa S3 (female), RPE-1 (female), 293T (female), and 293GP (female) cells were cultured in Dulbecco's modified Eagle medium (DMEM, Gibco) supplemented with 10% tetracycline-free fetal bovine serum (Omega Scientific) and 100 U mL^{-1} penicillin–streptomycin. PC3 (male) and COLO320DM (female) cells (a gift from Sihan Wu) were cultured in DMEM/F-12 (Gibco) supplemented with 10% tetracycline-free fetal bovine serum (Omega Scientific) and 100 U mL^{-1} penicillin–streptomycin. RPE-1 cells expressing a dominant-negative TRF2 allele (T2p1) were a gift from John Maciejowski. Cell lines were authenticated by karyotyping and were routinely confirmed to be free of mycoplasma contamination using the Universal Mycoplasma Detection Kit (ATCC). M229, M249, and M395 melanoma cell lines were established from patient-derived tumors at the University of California, Los Angeles with approval by the Institutional Review Board and maintained in high-glucose DMEM (Gibco) supplemented with 10% heat-inactivated fetal bovine serum (Gibco) and 2 mM glutamine. Melanoma cell lines were routinely tested for mycoplasma and profiled using a GenePrint 10 System (Promega).

METHOD DETAILS

Cell culture and reagents

Retroviral vectors were packaged into viruses by co-transfection of 293GP cells with pVSV-G (Addgene 139479). Viral supernatants were collected 48 or 72 hr post-transfection and filtered with a 0.45 μm syringe filter. Cells were transduced with retroviruses in the presence of 8 μg/mL polybrene (Sigma-Aldrich). For expression of pBABE-RFP-NLS, pBABE-GFP-SLX4 WT and L530A/W531A (a gift from Daniel Durocher), and pMMP-FLAG-FANCD2 WT and K561R (a gift from Gary Kupfer), cells were selected with puromycin for 48 hr following transduction. For expression of pQCXIB-mCherry-H2B and pQCXIB-mCherry-LMNB2 (a gift from Emily Hatch), cells were transduced and sorted for mCherry-positive cells by fluorescence-activated cell sorting (FACS). Correct localization of RFP-NLS, mCherry-H2B, GFP-SLX4, and mCherry-LMNB2 were confirmed in single-cell clones by microscopy.

Doxycycline (DOX) and auxin (IAA) (Millipore-Sigma) were dissolved in cell culture grade water and used at 1 μg/mL and 500 μM, respectively. Geneticin (G418 sulfate) and zeocin (InvivoGen) were used at selection concentrations of 300 and 50 μg/mL, respectively. Where indicated, cells were arrested with 100 ng/mL nocodazole (Millipore-Sigma) or 100 ng/mL colcemid (KaryoMAX, Thermo Fisher Scientific). To induce chromosome segregation errors, cells were treated with 100 ng/mL nocodazole (Millipore-Sigma), 500 nM Mps1 inhibitor (reversine, Cayman Chemical), or 1 μM Mps1 inhibitor (NMS-P715, Cayman Chemical). Mitomycin C (Sigma-Aldrich) was used at 50 nM or at the indicated concentration. EdU (Invitrogen) was used at 10 μM. Methotrexate (Calbiochem) was used at 50 nM. To induce common fragile site expression, aphidicolin (Cayman Chemical) was used at 50 nM. To induce genome-wide chromosome pulverization, the WEE1 inhibitor AZD-1775 (MedChemExpress) was used at 500 nM. To induce dicentric chromosome bridges, RPE-1 TRF2-DN cells were treated with 1 μg/mL DOX for 24 hr followed by a 24 hr washout. M229 and M395 melanoma cell lines were treated with 0.5 μM of the BRAF inhibitor vemurafenib (PLX4032, LC Laboratories) and 0.5 μM of the MEK inhibitor selumetinib (AZD6244, Selleck Chemicals) dissolved in DMSO; M249 was treated with 0.25 μM vemurafenib and 0.25 μM selumetinib.

CRISPR editing

Since most antibiotic selection markers have been used for previous genome editing steps to generate the DLD-1 CEN-SELECT cell line, we first inactivated a previously integrated puromycin resistance gene by cloning an sgRNA into the BbsI site of PX458 (Addgene 48138). DLD-1 cells were transfected with plasmid using X-tremeGENE 9 (Roche). After 3 days, GFP-positive single cells were isolated by FACS into individual wells of a 96-well plate. Single-cell derived clones were duplicated and one set was used to screened for sensitivity to 2 μg/mL puromycin.

To generate single-guide KO cell populations, CRISPR sgRNAs were designed using CRISPick (Broad Institute) and cloned into the BsmBI site of LentiCRISPRv2-Puro (Addgene 52961). Plasmids were packed into lentiviruses by co-transfection of 293T cells with pMD2.G (Addgene 12259) and psPAX2 (Addgene 12260). Viral supernatants were collected 48 hr post-transfection and filtered with a 0.45 μm syringe filter. Cell lines were transduced with virus in the presence of 8 μg/mL polybrene (Sigma-Aldrich). 48 hr post transduction, cell lines were selected with puromycin for 5 days (DLD-1, 2 μg/mL; HeLa, 2 μg/mL; RPE-1, 18 μg/mL). Cells were analyzed by immunoblotting either 7 days post-transduction or following completion of selection.

To generate dual-guide KO cell populations, CRISPR sgRNAs were designed using CRISPick (Broad Institute) and cloned into the BsmBI site of LentiCRISPRv2-Puro (Addgene 52961) and LentiGuide-Zeo (Addgene 160091). Lentiviruses were generated in 293T cells as previously described[18] and DLD-1 cells were co-transduced in the presence of 8 μg/mL polybrene (Sigma-Aldrich). Cells were co-selected 48 hr post-transduction with 2 μg/mL puromycin and 50 μg/mL of zeocin for 2 weeks. Modified cells were analyzed by immunoblotting following selection.

To generate single cell-derived KO clones, CRISPR sgRNAs were designed using CRISPick (Broad Institute) and cloned into the BsmBI site of PX459 (Addgene 62988). Plasmids were transfected into DLD-1 cells using X-tremeGENE 9 (Roche). For control guides, cells were selected in puromycin for 48 hr, expanded, and used as a control population. For targeting guides, 24 hr post transfection, cells were selected in puromycin for 48 hr. Single cells clones were then derived, expanded, and characterized by immunoblotting and/or amplicon sequencing. A list of oligonucleotides used in this study are provided in Table S2.

CRISPR-Cas9 screening

DNA Damage Response MKOv4 Library[42] (Addgene 140219) was amplified in ElectroMAX STBL4 cells (Invitrogen) and packaged into lentiviruses by co-transfection of 293T cells with pMD2.G (Addgene 12259) and psPAX2 (Addgene 12260). Viral supernatants were collected 48 hr post-transfection and filtered with a 0.45 μm syringe filter. DLD-1 CEN-SELECT cells were transduced with lentiviruses at low multiplicity of infection (MOI ~0.3). Cells were selected with 2 ug/mL puromycin 48 hr post-transduction. After 6 days, cells were split into two arms of 45 million cells each. The next day, DOX (1 μg/mL) and IAA (500 mM) were added to one arm and the other received vehicle only. After 3 days of DOX/IAA, cells were washed 3x with PBS and supplemented with fresh growth media. Following a 3-day recovery period, 300 ng/mL G418 was added to each arm, which were continually passaged in G418 for up to 25 days while maintaining a minimum of 45 million cells per arm. After 3 weeks, 4.5 million cells per arm were pelleted, and genomic DNA was isolated using Quick-DNA Midiprep Plus Kit (Zymo Research). sgRNA sequences were then amplified and prepared for next-generation sequencing according to protocols from the Broad Institute Genetic Perturbation Platform (https://portals.broadinstitute.org/gpp/public/resources/protocols).

Sequencing counts from the CRISPR screens were aligned and processed using custom Python-based scripts (https://github.com/mhorlbeck/ScreenProcessing), as previously described.[76,77] DNA Damage Response MKOv4 Library positive control genes (core essential genes) were grouped with the targeting genes for the analysis. sgRNA growth phenotypes were calculated by normalizing sgRNA $\log_2$ enrichment from T0 to endpoint samples. Gene phenotypes were scored based on the average phenotype of the 3 strongest sgRNAs (by absolute value). Mann-Whitney test p-values were calculated by comparing all sgRNAs targeting a given gene to the full set of negative control sgRNAs. Screen hits were defined as those genes where the absolute value of the calculated phenotype over the standard deviation of all evaluated phenotypes multiplied by the $\log_{10}$ of the Mann-Whitney p-value is greater than 5 (such that the false discovery rate [FDR] < 0.05). Gene ontology analysis of significantly enriched genes was performed using Metascape[75] with standard parameters.

Immunofluorescence and EdU staining

Cells seeded onto glass coverslips were fixed with 4% formaldehyde for 10 min at RT. For immunofluorescence of mitotic chromosomes, cells were collected by mitotic shake-off, pelleted, and swelled with 75 mM KCl for 15 min. Cells were then centrifuged onto glass slides using a Cytospin 4 cytocentrifuge (Thermo Fisher) at 366 RCF for 10 min. Cells were then fixed for 10 min with 4% formaldehyde and permeabilized with 0.3% Triton-X-100 in PBS for 5 min. Cells were then blocked for 1 hr with Triton Block (0.2 M glycine, 2.5% fetal bovine serum, 0.1% Triton-X-100, in PBS). For experiments including EdU labeling, click chemistry was performed prior to incubation in primary antibody according to manufacturer's protocol (Invitrogen). The following primary antibodies were diluted in Triton Block and incubated for 1 hr at RT or overnight at 4°C: anti-FANCD2 1:1,000 (Novus NB100-182), anti-FANCD2 1:100 (Santa Cruz sc-20022), anti-phospho-histone H2A.X (Ser139) 1:1,000 (Cell Signaling 2577), anti-phospho-histone H2A.X (Ser139) 1:1,000 (Sigma-Aldrich 05-636), anti-RPA32/RPA2 1:250 (Cell Signaling 2208), anti-53BP1 1:500 (Novus NB100-304), anti-RB 1:500 (Cell Signaling 9309), and anti-BrdU 1:100 (BD Biosciences 347580). Cells were rinsed 3x with 0.1% Triton-X-100 in PBS followed by 3x 10 min washes. Alexa fluor-conjugated secondary antibodies were diluted 1:1,000 in Triton Block and incubated for 1 hr at RT. Cells were rinsed and washed 3x with 0.1% Triton-X-100 in PBS followed by counterstaining with DAPI for 5 min. Cells were then mounted with ProLong Gold antifade mounting solution.

For IF-FISH, cells were processed using immunofluorescence protocol followed by fixation in Carnoy's fixative (3:1 methanol:acetic acid) for 15 min. Cells were then dehydrated in 80% ethanol for 2 min and subsequently processed according to FISH protocol.

Non-denaturing BrdU

RPE-1 cells were labeled with BrdU (10 μM) for 24 hr. Following 24 hr incubation, an Mps1 inhibitor was added to the cell culture media with continued BrdU supplementation. Cells were fixed 24 hr later and processed for immunofluorescence as described above.

Metaphase spread preparation

Cells were treated with 100 ng/mL colcemid (KaryoMAX, Thermo Fisher) for 4 hr and harvested by trypsinization. For experiments with melanoma cell lines, cells were treated with 50 ng/mL colcemid (Sigma) for 6 hr for control cells or 24 hr for MAPKi-treated cells. Cells were pelleted, then resuspended in 75 mM KCl solution dropwise with gentle agitation by vortexing. Cells were then incubated for 6 min at 37°C and fixed using fresh ice-cold Carnoy's fixative (3:1 methanol:acetic acid). Cells were pelleted and resuspended in appropriate volume of Carnoy fixative. Cells were dropped onto glass slides and air dried.

For melanoma experiments stained with YOYO-1, metaphase spreads were briefly rinsed in water and incubated with 0.4% Triton X-100 for 15 min. After washing with PBS, slides were incubated with 1 μM YOYO-1 (Invitrogen) for 30 min. Slides were then washed with PBS and mounted in ProLong Diamond antifade solution (Invitrogen). Images were acquired on a Leica SP8 confocal microscope system.

DNA fluorescence in situ hybridization (FISH)

DNA FISH probes (MetaSystems) were applied to metaphase spreads and sealed with a coverslip using rubber cement. Slides were co-denatured at 75°C for 2 min on a heat block and hybridized in a humidified chamber at 37°C overnight. Following hybridization, coverslips were carefully removed, and slides were washed with 0.4X SSC at 72°C for 2 min. Slides were then washed in 2X SSC with 0.05% Tween-20 at RT for 30 sec. Slides were counterstained with DAPI and mounted in ProLong Gold antifade solution. For multiplex-FISH, metaphase spreads were subjected to staining with Metasystems 24XCyte DNA FISH probes. Images were captured using the Metafer Scanning and Imaging Platform (Metasystems) as previously described.[18,20] Images were analyzed using the Isis Fluorescence Imaging Platform (Metasystems). For DNA FISH targeting the *DHFR* locus, RP11-90A9 bacterial artificial chromosomes (BACs) were obtained from BACPAC Resources (https://bacpacresources.org), isolated using a NucleoBond Xtra BAC kit (Macherey-Nagel), and prepared using the Nick Translation DNA Labeling System 2.0 (Enzo Life Sciences).

For melanoma experiments, metaphase spreads were dehydrated in 70%, 85% and 100% ethanol for 2 min each. *BRAF*/CEN7 FISH probes (Empire Genomics) were mixed with hybridization buffer in 1:4 ratio and applied to spreads. Slides were sealed with a coverslip using rubber cement and denatured at 73°C for 2 min. Hybridization was performed overnight at 37°C in a humidified chamber. After removing the rubber cement and coverslip, the slides were washed in 0.4X SSC/0.3% IGEPAL at 73°C for 2 min, followed by another 2 min wash with 2x SSC/0.1% IGEPAL at room temperature. Slides were mounted and counterstained with

ProLong Diamond antifade solution with DAPI (Invitrogen). Images were acquired on a Leica SP8 confocal microscope system.

Y chromosome shattering and rearrangement assays

To analyze Y chromosome shattering, metaphase spreads were prepared from DLD-1 cells after 3 days of DOX/IAA treatment, as previously described.[6,78] To analyze Y chromosome rearrangements, DLD-1 cells were treated with DOX/IAA for 3 days, washed 3x with PBS, and then cultured for an additional 3 days. Cells were then selected with 300 ng/mL G418 for 2 weeks. Following treatment, cells were arrested with colcemid and processed for metaphase spreads. Metaphase spreads were then subjected to DNA FISH with two-color paint probes (Metasystems), as previously described.[7,20,78] For chromosome shattering assays, images were manually inspected using Fiji (v.2.1.0/1.53c) and scored for both fragmentation frequency and the number of fragments per cell. Cells harboring 3 or more microscopically visible fragments were considered shattered. For rearrangement analysis, images were manually inspected using previously described criteria.[7,20,78]

Fluorescence microscopy

Immunofluorescence and metaphase DNA FISH experiments were imaged on a DeltaVision Ultra (GE Healthcare) microscope system equipped with 4.2 MPx sCMOS detector. Images of interphase cells and metaphase spreads were acquired with a 100X oil objective (1.4 NA, Olympus UPlanSApo) and deconvolved using softWorX program (v.7.2.1, Cytiva). Mitotic cells were imaged with 15 x 0.2 μm z-sections and deconvolved maximum intensity projections were generated using softWoRx program.

Immunoblotting

Cells were harvested by scraping, lysed in 2X SDS sample buffer, and denatured at 95°C for 5 min. Lysates were then cleared by centrifugation (14,000 RCF for 15 min) and quantified using a BCA assay kit (Pierce). Loading buffer was added and samples were boiled for 10 min at 95°C. For melanoma cell lines, cells were lysed in RIPA buffer (Thermo Fisher) with protease inhibitor cocktail (Thermo Fisher) and phosphatase inhibitor cocktails (Thermo Fisher). Samples were resolved by SDS polyacrylamide gel electrophoresis and transferred onto 0.2 μm PVDF membranes. Membranes were then incubated with 5% milk in PBST (0.1% Tween-20 in PBS) for 1 hr. The following primary antibodies were diluted in 5% milk in PBST and incubated with membrane overnight at 4°C: anti-FANCD2 1:1,000 (Novus NB100-182), anti-XPF/ERCC4 1:1,000 (Bethyl A301-315A), anti-LMNB1 1:1,000 (Proteintech 12987-1-AP), anti-POLD3 1:500 (Abnova M01), anti-TREX1 1:1,000 (Cell Signaling 15107), anti-MPG 1:1,000 (Novus NBP1-82787), anti-β-actin 1:2,000 (Cell Signaling 4970), and anti-α-tubulin 1:1,000 (Cell Signaling 2144S). Following overnight incubation, the membrane was rinsed 3x with PBST and washed 3x 15 min. HRP-conjugated secondary antibodies (Invitrogen) were diluted in 5% milk in TBST and incubated with membrane for 1 hr at RT. Membrane was rinsed 3x with PBST and washed 3x 15 min followed by detection with SuperSignal West Pico Plus chemiluminescent substrate (Thermo Scientific) and imaged using ChemiDox MP imaging system (Bio-Rad).

QUANTIFICATION AND STATISTICAL ANALYSIS

Statistical tests were performed as described in the figure legends using GraphPad Prism version 9.5.0. Sample sizes, statistical analyses, significance values are reported in the figure legends, denoted in the figure panel, or described in the text. Definitions for n are described in the figure legends. All experiments were performed independently at least three times unless otherwise indicated. For statistical analyses, $P > 0.05$ were considered not significant (ns), and asterisks denote the following: $^{*}P \leq 0.05$; $^{**}P \leq 0.01$; $^{***}P \leq 0.001$; $^{****}P \leq 0.0001$. Error bars represent standard error mean (SEM) unless otherwise indicated.

CellPress

Supplemental figures

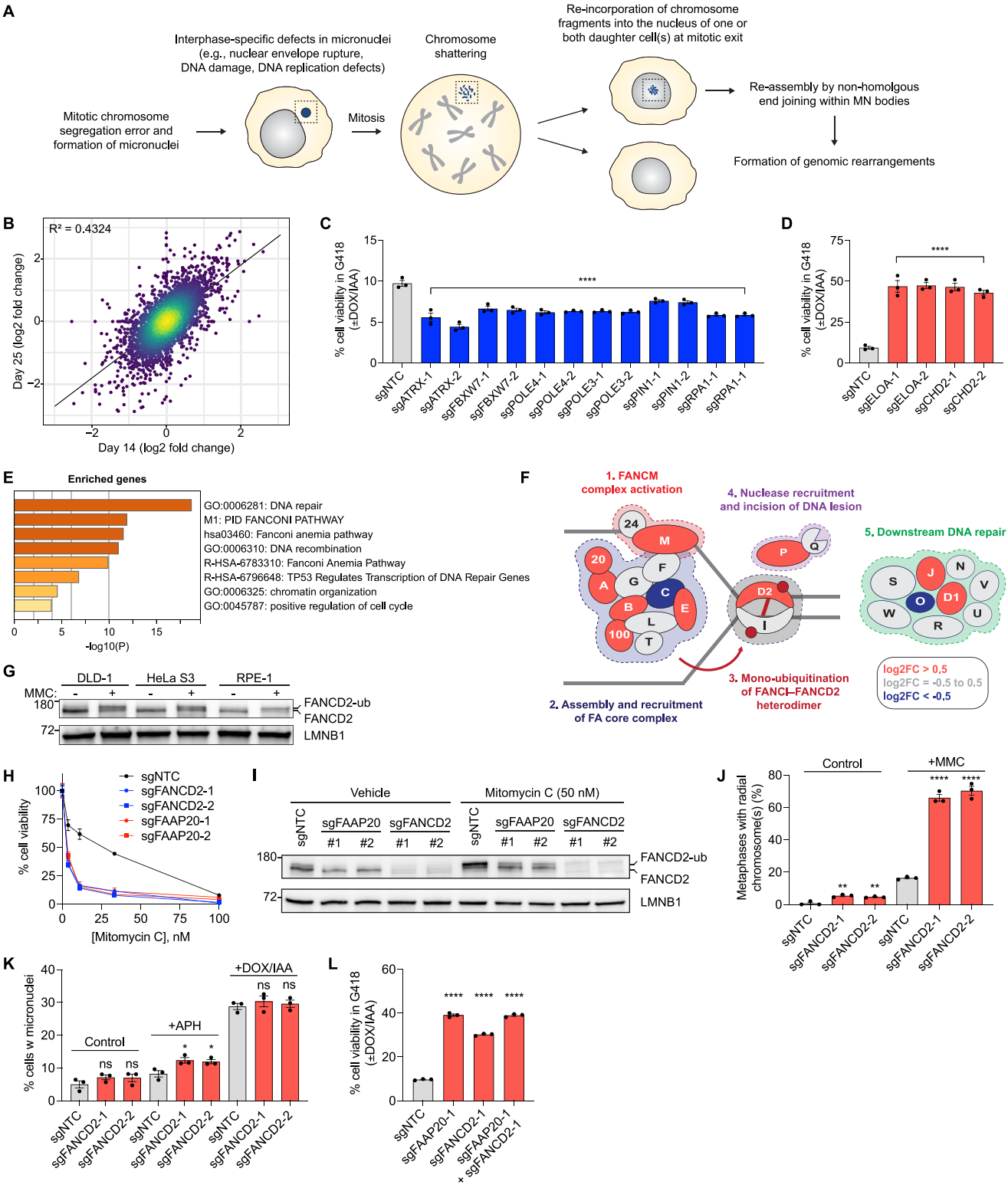

(legend on next page)

Figure S1. Validation of CRISPR-Cas9 screen to identify regulators of chromothripsis, related to Figure 1

(A) Schematic overview of the cascade to chromothripsis originating from initial errors in mitosis that produce micronuclei. Chromosomes encapsulated within micronuclei are susceptible to catastrophic shattering and reassembly by intrinsic DNA repair mechanisms, generating a spectrum of genomic rearrangements that are restricted to individual chromosomes. In a CRISPR screen, inactivating genes involved at any step is expected to block the cascade, resulting in chromothripsis.

(B) Scatterplot comparing fold change (±DOX/IAA) of individual sgRNAs on day 14 versus day 25. Line represents linear regression with $R^2 = 0.4324$.

(C and D) CEN-SELECT growth assay in CRISPR-Cas9-mediated KO populations using 2 independent sgRNAs for a subset of top depleted (C) or enriched (D) genes. Data represent mean ± SEM of $n = 3$ experiments; statistical analyses by ordinary one-way ANOVA test with multiple comparisons.

(E) Ontology analysis of significantly enriched genes.

(F) Color-coded annotations of the canonical FA pathway according to their respective $\log_2$ fold change values at the 25-day time point.

(G) Immunoblot of FANCD2 mono-ubiquitination in the indicated cell lines treated with or without 500 nM MMC for 24 h.

(H) Cell viability of FANCD2 and FAAP20 KO DLD-1 cells subjected to escalating doses of MMC for 7 days. Data represent mean ± SEM of $n = 3$ experiments each performed in triplicate.

(I) Immunoblot confirming FANCD2 KO and mono-ubiquitination defect in FANCD2 and FAAP20 KO DLD-1 populations treated with control or 50 nM MMC for 24 h.

(J) Quantification of metaphase spreads with one or more radial chromosome(s) from DLD-1 cells treated with or without 50 nM MMC for 24 h. Data represent mean ± SEM of $n = 3$ experiments analyzing 144–183 metaphase spreads.

(K) Quantification of micronuclei in DLD-1 cells treated with 50 nM APH for 24 h or DOX/IAA for 72 h. Data represent mean ± SEM of $n = 3$ experiments analyzing 786–1,069 interphase cells.

(L) CEN-SELECT growth assay in single or double KO DLD-1 cells. Data represent mean ± SEM of $n = 3$ experiments; statistical analyses in (J)–(L) by ordinary one-way ANOVA test with multiple comparisons.

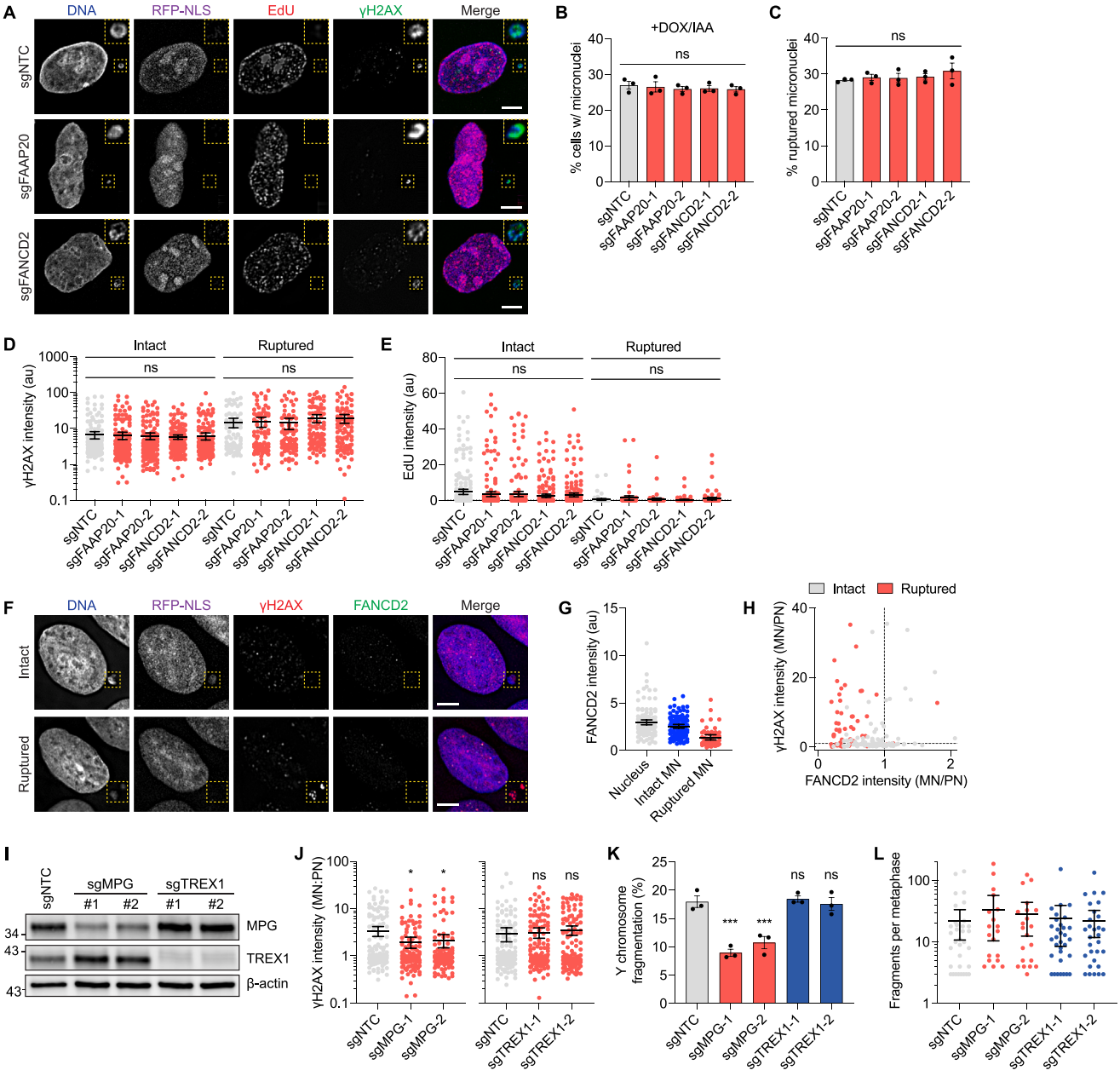

Figure S2. The FA pathway does not contribute to micronuclear envelope rupture or interphase DNA damage and DNA replication defects in micronuclei, related to Figure 1

(A) Representative images of DNA damage (accumulation of γH2AX) and DNA replication defects (lack of EdU incorporation) in ruptured micronuclei from FANCD2 and FAAP20 KO DLD-1 cells. Cells pulsed with EdU for 1 h prior to fixation. Scale bars, 5 μm.

(B) Quantification of the proportion of cells with micronuclei upon DOX/IAA induction. Data represent mean ± SEM of $n = 3$ experiments analyzing 992–1,149 cells.

(C) Frequency of micronucleus envelope rupture as determined by the loss of RFP fused to a nuclear localization signal (RFP-NLS). Data represent mean ± SEM of $n = 3$ experiments analyzing 269–311 micronuclei; statistical analyses in (B) and (C) by ordinary one-way ANOVA test with multiple comparisons.

(D) Mean intensity of γH2AX in intact (RFP-NLS+) and ruptured (RFP-NLS−) micronuclei.

(E) Mean intensity of EdU in intact (RFP-NLS+) and ruptured (RFP-NLS−) micronuclei. Data in (D) and (E) represent mean ± 95% CI from $n = 77–220$ micronuclei pooled from 3 experiments; statistical analyses by non-parametric Kruskal-Wallis test with correction for multiple comparisons.

(F) Representative examples of interphase DLD-1 cells expressing RFP-NLS and immunostained for γH2AX and FANCD2. Scale bars, 5 μm.

(G) Nuclear and micronuclear FANCD2 mean intensity. Data represent mean ± 95% CI from $n = 54–133$ nuclei or micronuclei pooled from 3 experiments.

(H) Quantification of γH2AX and FANCD2 between micronuclei (MN) and their corresponding primary nucleus (PN). Data represent the mean intensity MN/PN ratio pooled from $n = 113$ intact micronuclei and $n = 55$ ruptured micronuclei.

(I) Immunoblot confirming CRISPR-Cas9-mediated MPG and TREX1 KO 7 days post-lentiviral transduction.

(legend continued on next page)

(J) Ratio of MN/PN γH2AX intensity in MPG or TREX1 KO DLD-1 cells treated with DOX/IAA for 48 h. Data represent the MN/PN ratio of mean intensity from *n* = 134–155 micronuclei pooled from 3 experiments; statistical analysis by non-parametric Kruskal-Wallis test with correction for multiple comparisons.
(K) Y chromosome shattering following DOX/IAA induction for 72 h. Data represent mean ± SEM of *n* = 3 experiments analyzing 258–317 metaphases; statistical analysis by ordinary one-way ANOVA test with multiple comparisons.
(L) Number of fragments per metaphase containing a shattered Y chromosome from (K). Data represent the mean ± 95% CI from *n* = 19–34 metaphases pooled from 3 experiments.

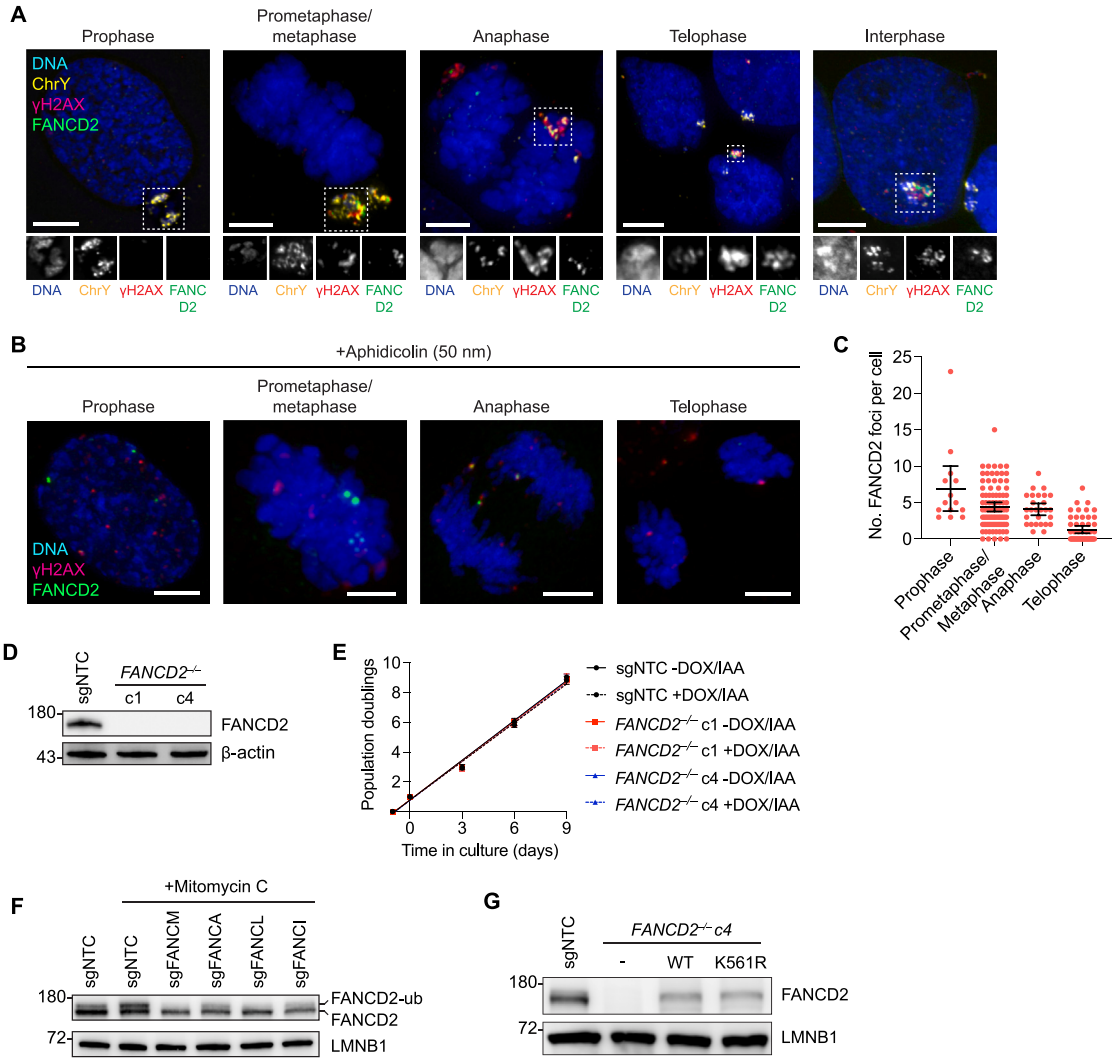

Figure S3. Characterization of mitotic FANCD2 recruitment and FA-deficient DLD-1 cells, related to Figure 2

(A) Representative images of DLD-1 cells at the indicated mitotic stages with or without co-localization of FANCD2 with shattered Y chromosomes. Scale bars, 5 μm.

(B) Representative images of DLD-1 cells at the indicated mitotic stages with APH-induced FANCD2 foci. Scale bars, 5 μm.

(C) Quantification of FANCD2 foci from (B). Data represent mean ± 95% CI from *n* = 14–91 cells pooled from 3 experiments.

(D) Immunoblot for FANCD2 in two independent *FANCD2*$^{-/-}$ DLD-1 clones generated by CRISPR-Cas9 editing.

(E) Population doublings of *FANCD2*$^{-/-}$ DLD-1 clones with and without DOX/IAA induction. Data represent linear regression line from *n* = 3 experiments performed in technical triplicate.

(F) Immunoblot of MMC-induced FANCD2 mono-ubiquitination in the indicated DLD-1 KO populations.

(G) Immunoblot of *FANCD*$^{-/-}$ DLD-1 clone expressing FANCD2 WT and ubiquitination-deficient mutant (K561R) rescue.

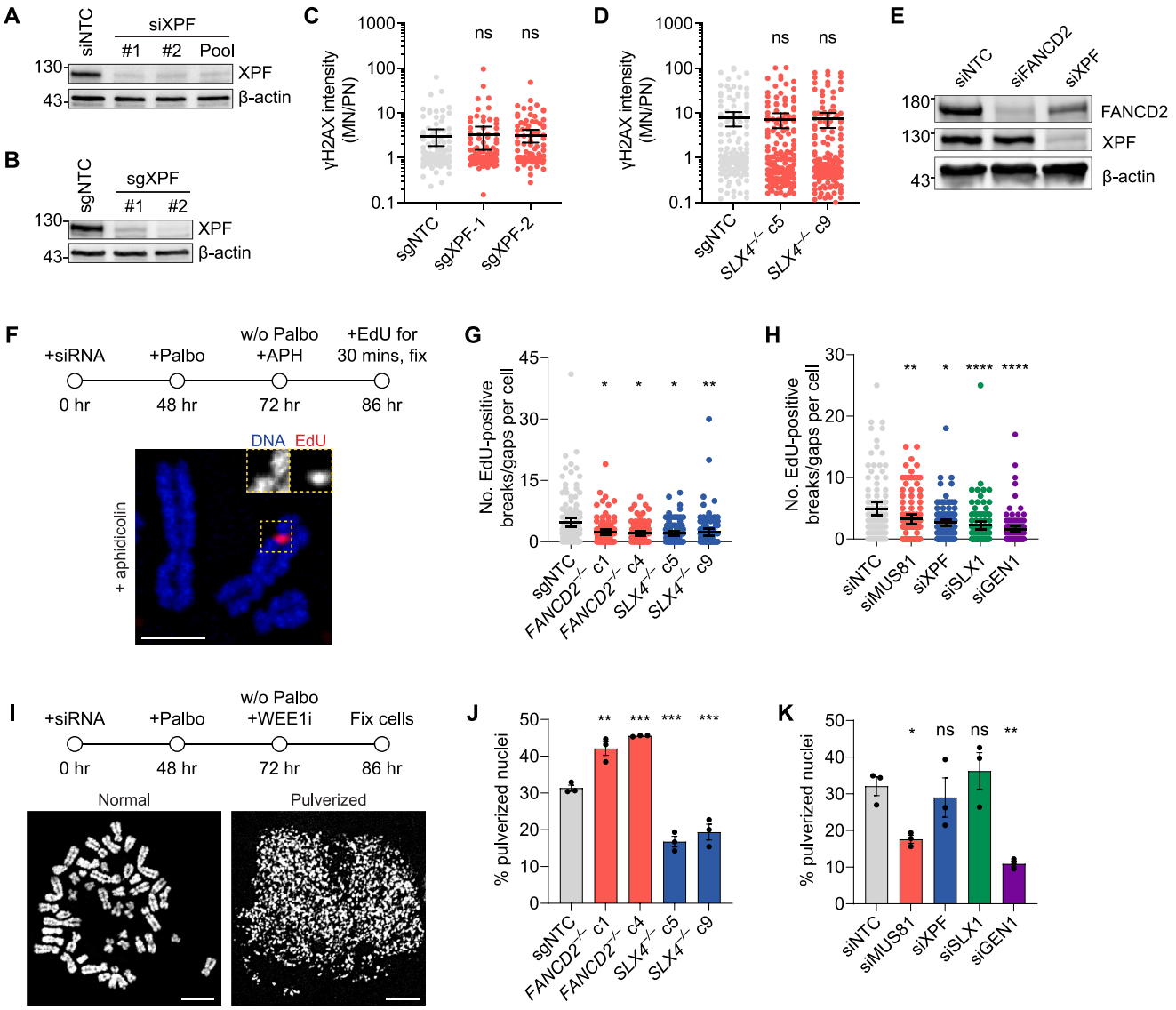

Figure S4. FA-induced chromothripsis is distinct from common fragile site expression and premature condensation-induced genome pulverization, related to Figure 3

(A) Immunoblot confirming depletion of XPF in DLD-1 cells 72 h post-transfection with the indicated siRNAs.

(B) Immunoblot confirming XPF KO in DLD-1 cells 7 days post-transduction with the indicated sgRNAs.

(C) Ratio of micronuclear to nuclear (MN/PN) γH2AX intensity in XPF KO DLD-1 cells treated with DOX/IAA for 48 h. Data represent the MN/PN ratio of mean intensity from *n* = 122, 122, and 114 micronuclei pooled from 3 experiments.

(D) Ratio of MN/PN γH2AX intensity in *SLX4*$^{-/-}$ DLD-1 clones treated with DOX/IAA for 48 h. Data represent the MN/PN ratio of mean intensity from *n* = 147–153 micronuclei pooled from 3 experiments; statistical analyses in (C) and (D) by non-parametric Kruskal-Wallis test with correction for multiple comparisons.

(E) Immunoblot confirming depletion of FANCD2 or XPF in RPE-1 cells 72 h post-transfection with the indicated siRNAs.

(F) Experimental schematic and representative image of APH-induced MiDAS at a chromosome break/gap. DLD-1 cells were synchronized in G1 with palbociclib for 24 h, released into 50 nM APH for 16 h, and pulsed with EdU and nocodazole for 30 min prior to collection of metaphase spreads. Scale bars, 5 μm. Palbo, palbociclib; w/o, washout.

(G) Number of EdU+ breaks/gaps following the treatment conditions described in (F) for the indicated genotypes. Data represent mean ± 95% CI from *n* = 91–113 metaphases pooled from 3 experiments.

(H) Number of EdU+ breaks/gaps following the treatment conditions described in (F) 48 h post-transfection with the indicated siRNAs. Data represent mean ± 95% CI from *n* = 97–104 metaphases pooled from 3 experiments. Statistical analyses in (G) and (H) by non-parametric Kruskal-Wallis test with correction for multiple comparisons.

(I) Experimental schematic and representative images of WEE1 inhibitor (WEE1i)-induced chromosome condensation and genome pulverization in DLD-1 cells. Scale bars, 10 μm.

(legend continued on next page)

(J) Quantification of nuclei with a pulverized appearance as in (I) for the indicated genotypes. Data represent mean ± SEM of $n = 3$ experiments analyzing 118–193 nuclei.

(K) Quantification of nuclei with a pulverized appearance as in (I) 48 h post-transfection with indicated siRNAs. Data represent mean ± SEM of $n = 3$ experiments analyzing 177–199 nuclei. Statistical analyses in (J) and (K) by ordinary one-way ANOVA test with multiple comparisons.

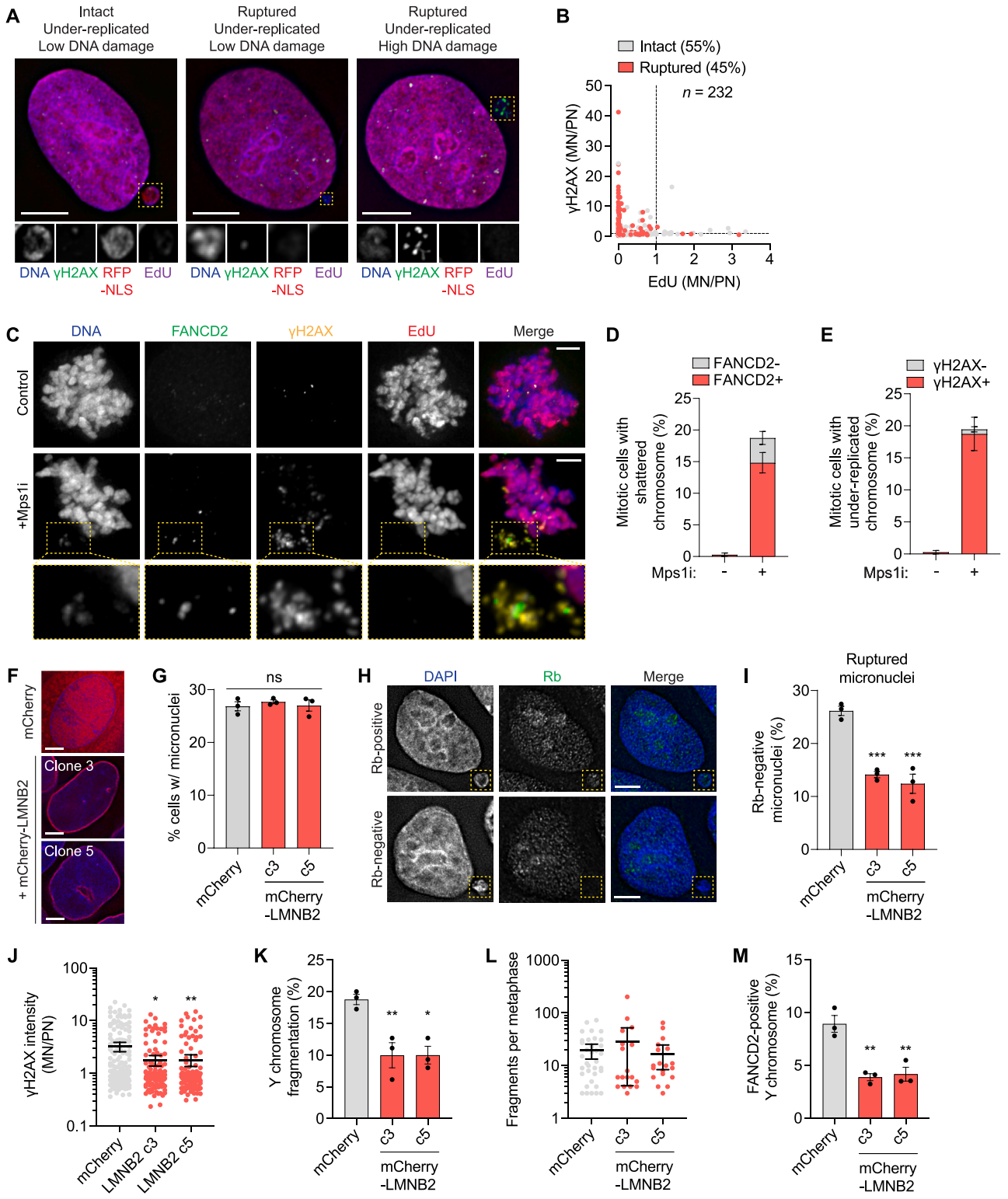

Figure S5. Mitotic shattering of under-replicated chromosomes from ruptured micronuclei, related to Figure 4

(A and B) Representative images (A) and quantification (B) of EdU and γH2AX in 48 h DOX/IAA-treated DLD-1 cells expressing RFP-NLS. Cells were synchronized in G1 with palbociclib (24 h) and released into EdU-containing media for 16 h. Each data point represents the MN/PN ratio of EdU and γH2AX mean intensity for a single intact or ruptured micronucleus; *n* = 232 micronuclei pooled from 3 experiments. Scale bars, 5 μm.

(legend continued on next page)

(C) Representative images of Mps1 inhibitor-treated RPE-1 cell with under-replicated and under-condensed DNA characterized by weak DAPI staining with FANCD2 and γH2AX. Scale bars, 5 μm.
(D) FANCD2 recruitment to shattered chromosomes from (C). Data represent mean ± SEM of *n* = 3 experiments analyzing 256–274 mitotic cells.
(E) γH2AX status of under-replicated chromosomes from micronuclei in RPE-1 cells treated with an Mps1 inhibitor. Data represent mean ± SEM of *n* = 3 experiments analyzing 256–274 mitotic cells.
(F) Representative image of DLD-1 cells expressing mCherry or two independent clones expressing mCherry-LMNB2. Scale bars, 5 μm.
(G) Proportion of cells with micronuclei upon DOX/IAA induction. Data represent mean ± SEM of *n* = 3 experiments analyzing 555–616 cells.
(H and I) Representative images (H) and quantification (I) of Rb immunostaining in DOX/IAA-induced DLD-1 derivative cell lines. Data represent mean ± SEM of *n* = 3 experiments analyzing 253–325 cells. Scale bars 5 μm in (H).
(J) Ratio of MN/PN γH2AX intensity in DLD-1 derivative cell lines treated with DOX/IAA for 48 h. Data represent the mean MN/PN ratio ± 95% CI from *n* = 134–170 micronuclei pooled from 3 experiments; statistical analysis by non-parametric Kruskal-Wallis test with correction for multiple comparisons.
(K) Y chromosome-shattering analysis by metaphase FISH following DOX/IAA induction for 72 h. Data represent mean ± SEM of *n* = 3 experiments analyzing 313–317 metaphases.
(L) Number of fragments per metaphase containing a shattered Y chromosome from (K). Data represent the mean ± 95% CI from *n* = 18–35 metaphases pooled from 3 experiments.
(M) FANCD2 localization to shattered Y chromosomes in DLD-1 derivative cell lines treated with DOX/IAA for 72 h. Data represent mean ± SEM of *n* = 3 experiments analyzing 226–257 mitotic cells.
Statistical analyses for (G), (I), (K), and (M) by ordinary one-way ANOVA test with multiple comparisons.

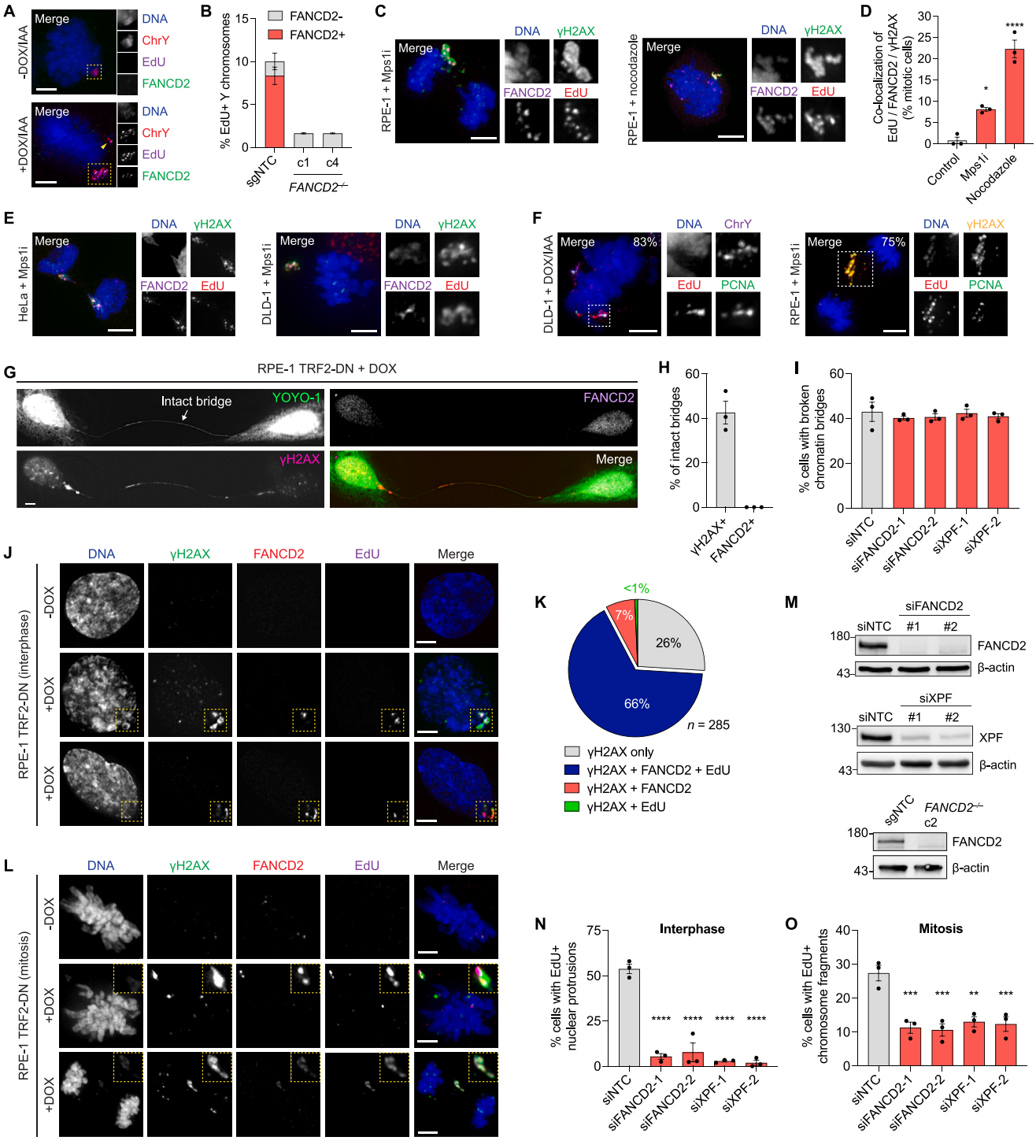

Figure S6. Mitotic recruitment of FANCD2 to micronucleated chromosomes and chromatin bridges undergoing aberrant DNA synthesis, related to Figure 4

(A) Representative IF-FISH images of 72 h DOX/IAA-treated DLD-1 cells pulsed with EdU for 30 min prior to fixation. Scale bars, 5 μm.

(B) Y-chromosome-specific EdU incorporation with or without FANCD2 localization in control DLD-1 cells or *FANCD2*$^{-/-}$ clones. Data represent the mean of $n = 3$ experiments analyzing 184–193 mitotic cells.

(C) Representative images of mitotic RPE-1 cells following the induction of micronuclei by 8 h treatment with an Mps1 inhibitor (left) or 8 h nocodazole arrest followed by mitotic shake-off and release into fresh media (right). Following 24 h recovery, cells were pulsed for 30 min with EdU prior to immunostaining for FANCD2 and γH2AX on misaligned chromosomes. Scale bars, 5 μm.

(legend continued on next page)

(D) Quantification of co-localization between FANCD2, γH2AX, and EdU from (C). Data represent mean ± SEM of *n* = 3 experiments analyzing 158–164 mitotic cells.
(E) Representative images of mitotic HeLa (left) and DLD-1 (right) cell treated with an Mps1 inhibitor for 8 h with co-localization between FANCD2 and EdU on shattered chromosomes. Scale bars, 5 μm.
(F) Representative images of 72 h DOX/IAA-treated DLD-1 cell (left) and 8 h Mps1-inhibitor-treated RPE-1 cell (right) showing mitotic co-localization of PCNA with EdU. Shattered chromosomes were identified by Y chromosome DNA FISH or immunostaining for γH2AX on misaligned or lagging chromosomes. Quantification represents the percentage of events in which EdU co-localizes with PCNA from *n* = 30 mitotic DLD-1 cells or 40 mitotic RPE-1 cells pooled from 2 experiments. Scale bars, 5 μm.
(G) Representative image of an intact interphase chromatin bridge from a doxycycline-inducible TRF2-DN RPE-1 cell without visible FANCD2. Scale bars, 5 μm.
(H) Intact chromatin bridges with detectable γH2AX or FANCD2. Data represent mean ± SEM of *n* = 3 experiments analyzing 99 bridges.
(I) Cells with broken chromatin bridges in doxycycline-induced RPE-1 TRF2-DN cells 72 h post-transfection with indicated siRNAs. Data represent mean ± SEM of *n* = 3 experiments analyzing 398–444 cells.
(J and K) Representative images (J) and quantification (K) of co-localization between γH2AX, FANCD2, and EdU on broken chromatin bridges during interphase in doxycycline-induced RPE-1 TRF2-DN cells pulsed with EdU for 30 min prior to fixation. Scale bars, 5 μm. Data represent the percentage of cells with broken bridges displaying co-localization of the indicated factors from *n* = 285 cells pooled from 3 independent replicates.
(L) Examples of the localization of γH2AX, FANCD2, and EdU to broken chromatin bridges during mitosis in doxycycline-induced RPE-1 TRF2-DN cells pulsed with EdU for 30 min prior to fixation. Scale bars, 5 μm.
(M) Immunoblots confirming FANCD2 and XPF knockdown 72 h post-transfection with the indicated siRNAs (top and middle) or FANCD2 knockout (bottom) in RPE TRF2-DN cells.
(N) Percentage of cells displaying broken chromatin bridges with EdU incorporation in doxycycline-induced RPE-1 TRF2-DN siRNA transfected cells pulsed with EdU for 30 min before fixation. Data represent mean ± SEM of *n* = 3 experiments analyzing 171–189 cells.
(O) Percentage of mitotic cells that display EdU incorporation in doxycycline-induced RPE-1 TRF2-DN siRNA-transfected cells pulsed with EdU for 30 min prior to fixation. Data represent mean ± SEM of *n* = 3 experiments analyzing 91–115 mitotic cells.
Statistical analyses in (D), (N), and (O) by ordinary one-way ANOVA test with multiple comparisons.

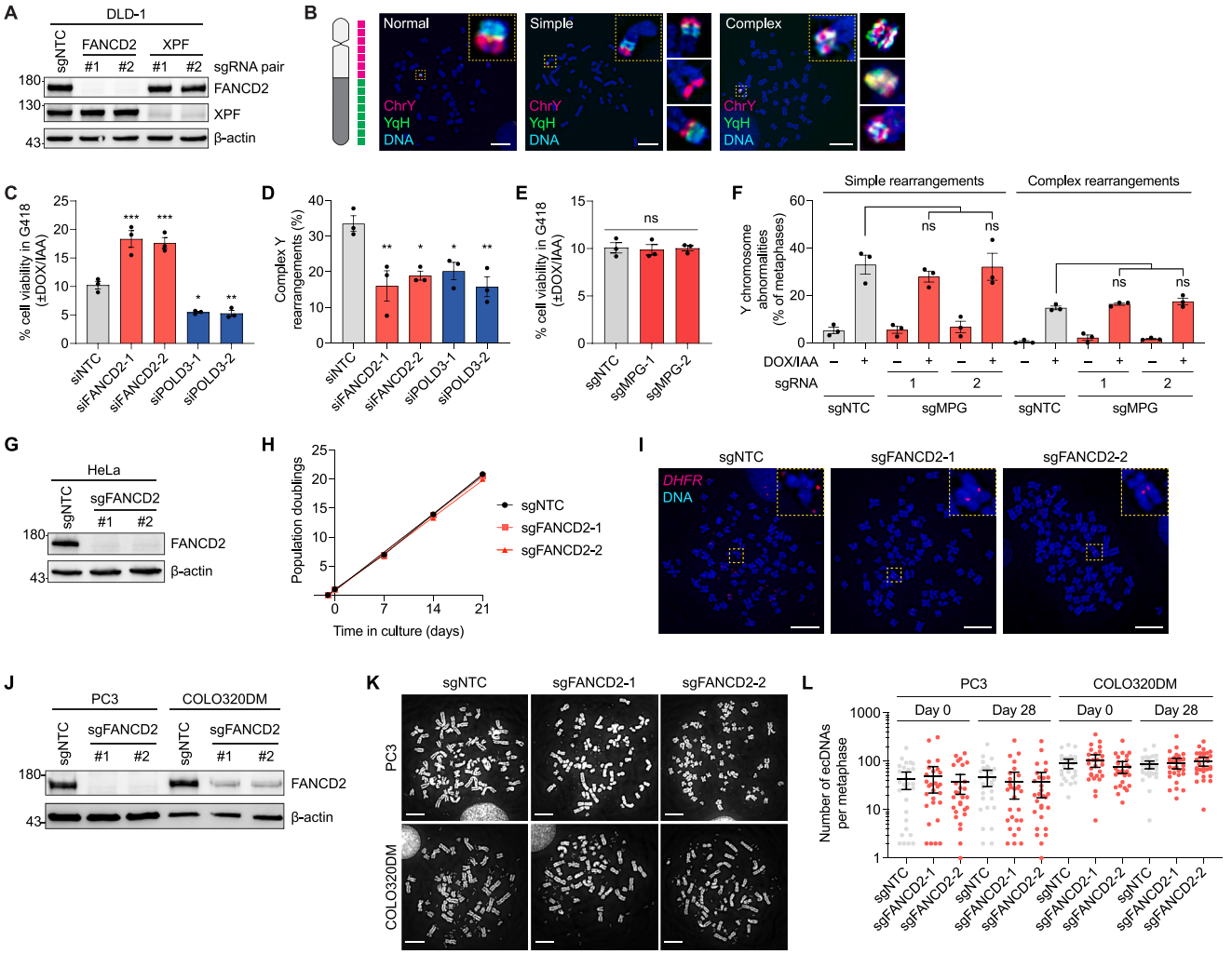

Figure S7. Characterization of genomic alterations in a panel of FA-deficient cell lines, related to Figure 6

(A) Immunoblot confirming efficiency of FANCD2 and XPF KO in DLD-1 cells 7 days post-transduction with the indicated sgRNA pairs.

(B) Schematic and representative examples of metaphase DNA FISH using dual-color painting probes to distinguish between normal and rearranged Y chromosomes. Scale bars, 10 μm.

(C) CEN-SELECT growth assay in DLD-1 cells transfected with indicated siRNAs. Data represent mean ± SEM from *n* = 3 experiments.

(D) Complex Y chromosome rearrangements following DOX/IAA induction and G418 selection. Data represent mean ± SEM of *n* = 3 experiments analyzing 215–295 metaphases.

(E) CEN-SELECT growth assay in MPG KO DLD-1 cells. Data represent mean ± SEM from *n* = 3 experiments.

(F) Y chromosome rearrangements following DOX/IAA induction and G418 selection. Data represent mean ± SEM of *n* = 3 experiments analyzing 186–298 metaphases.

(G) Immunoblot confirming FANCD2 KO in HeLa cells 7 days post-transduction.

(H) Proliferation rate of FANCD2 KO HeLa cells.

(I) Representative metaphase FISH images of MTX-resistant cells hybridized to BAC probes targeting the *DHFR* locus. Scale bars, 10 μm.

(J) Immunoblot of CRISPR-Cas9-mediated editing of FANCD2 in PC3 and COLO320DM cells 7 days post-transduction.

(K) Representative metaphase spreads of FANCD2 KO PC3 and COLO320DM cells following 28 days of culture. Scale bars, 10 μm.

(L) Number of ecDNAs per metaphase in FANCD2 KO PC3 and COLO320DM cells analyzing *n* = 28–30 metaphases pooled from 2 experiments.

Statistical analyses for (C)–(F) by ordinary one-way ANOVA test with multiple comparisons.

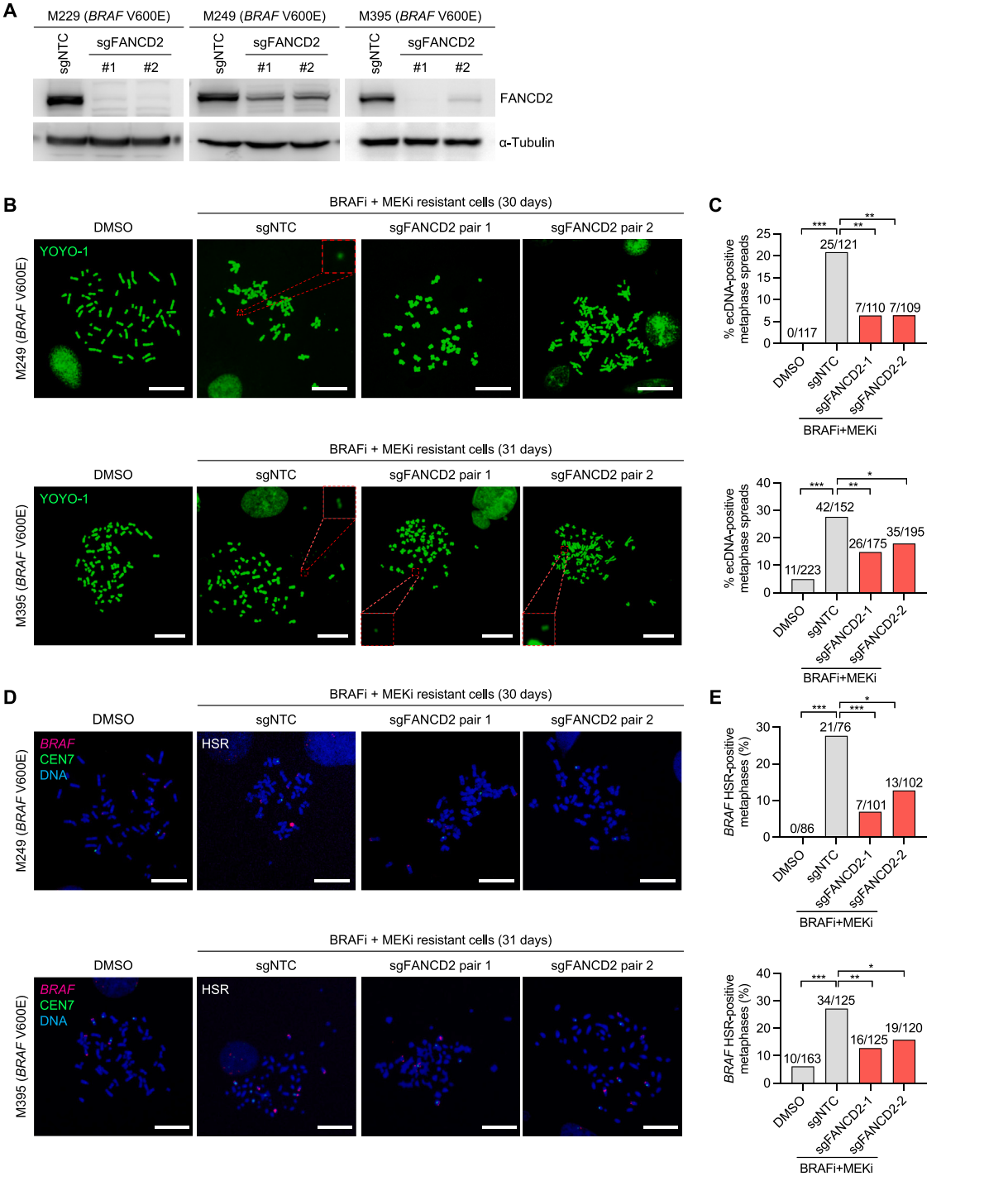

Figure S8. Inactivation of the FA pathway suppresses ecDNA-/HSR-mediated gene amplification and resistance to targeted therapy in BRAF V600E-mutant melanoma, related to Figure 6

(A) Immunoblot confirming loss of FANCD2 in the indicated *BRAF*-mutant melanoma cell lines.

(B) Representative images of metaphase spreads derived from the indicated cell lines treated with DMSO or BRAFi + MEKi for ~1 month and stained with YOYO-1 to detect ecDNAs. Scale bars, 20 μm.

(C) Quantification of metaphases with detectable ecDNA structures as visualized by YOYO-1 staining from (B). Data represent frequency from the indicated number of metaphases pooled from multiple plates as needed; statistical analysis by Fisher's exact test.

(legend continued on next page)

(D) Representative images of metaphase spreads derived from the indicated cell lines treated with DMSO or combination BRAFi + MEKi for ~1 month with or without *BRAF* HSRs as detected by FISH for the *BRAF* locus. CEN7, centromere of chromosome 7. Scale bars, 20 μm.
(E) Quantification of metaphases with detectable *BRAF*-positive HSRs as visualized by FISH from (D). Data represent frequency from the indicated number of metaphases pooled from multiple plates as needed; statistical analysis by Fisher's exact test.